Development of a Scintillating Fibre Tracker/Time-of-Flight Detector with SiPM Readout for the Mu3e Experiment at PSI

Antoaneta Damyanova

UNIVERSITÉ DE GENÈVE

Master Thesis

Supervisor: Dr Alessandro Bravar

June, 2013

Contents

Chapter 1

Introduction

The most successful theory in nowadays particle physics is the Standard Model. Eventhough, it adequately describes the building blocks of our world and their properties, it is an incomplete theory. Within its framework, questions like why the neutrinos have no mass and why gravity cannot be unified with the electromagnetic, weak and strong interactions remain opened. Various theories attempt to solve these problems, however, they also predict phenomena which have not been observed so far. An example is the lepton flavour violation in the charged lepton sector. In the Standard Model a lepton flavour violating process like $\mu^+ \rightarrow e^+e^-e^+$ is strongly suppressed and practically unobservable with present day technology. On the contrary, many of the beyond Standard Model theories foresee its existence at experientially accessible scales. Any discovery of such process, therefore, will be a clear evidence for new physics.

Mu3e is an experiment proposed to study the lepton flavour violating decay $\mu^+ \rightarrow e^+e^-e^+$ with a sensitivity of one in 10^{16} [1]. It aims either to make a new discovery or to improve the current experimental limit BR($\mu^+ \rightarrow e^+e^-e^+$)<1×10^{-12} at 90% C.L. [2] by four orders of magnitude. Both, positive or negative result, will refine and constrain the parameters of the theories beyond the Standard Model. To reach the desired sensitivity, a Mu3e detector should be capable of measuring precisely the momentum of individual particles. The experiment will operate at very high muon decay rates, so in addition to accurate vertex and momentum measurements, excellent time resolution is required. Scintillating fibres coupled to silicon photon detectors will be used in a timing hodoscope to provide the time information.

The subject of the present work is to investigate the feasibility of using such a scintillating fibre hodoscope in the Mu3e experiment. Scintillating fibres staggered into ribbons and read by silicon photomultipliers (SiPMs) were constructed. The author developed a method and produced the first ribbon prototypes which were later studied with a collimated radioactive source ^{90}Sr. Data acquired through CAMAC TDC and ADC modules was analysed offline. Efficiency and timing measurement were performed. A systematic study of the time resolution depending on the number of photons produced in the scintillating fibres is presented.

The results from the initial tests indicate that a system based on plastic scintillating fibres and readout by SiPMs could fulfil the requirements for a Mu3e time-of-flight detector.

Chapter 2

Theoretical Background

2.1 The Standard Model

The Standard Model is a quantum field theory that defines the properties of twelve elementary particles and their antiparticles and describes their interactions through the strong, electromagnetic and weak forces. The forces are mediated via particles called gauge bosons.

Within the Standard Model the elementary particles are classified as fermions since they are characterized by a half-integer spin. The gauge bosons, on the other hand, have an integer spin and they belong to the class of bosons. Depending on whether the particles interact strongly with each other or not they are further separated into families of quarks and leptons. The quarks family consists of six particles (and their antiparticles) known as up (u), down (d), strange (s), charm (c), top (t) and bottom (b) quarks. They interact via strong, electromagnetic and weak interactions. In the lepton family, however, the particles interact between each other only electromagnetically and weakly. There are six leptons which are called electron (e), electron neutrino (ν_e), muon (μ), muon neutrino (ν_μ), tau τ and tau neutrino (ν_τ). The matter particles are further grouped into three generations as indicated in Fig. 2.1. In the lepton sector to each generation is assigned a lepton flavour number. The electron e and the electron neutrino ν_e belong to the same generation, so they are both characterized by a lepton flavour number $L_e = 1$. Their antiparticles - the positron e^+ and the electron anti-neutrino $\bar{\nu}_e$ have the opposite value of the lepton flavour number i.e. $L_e = -1$. Similarly, the muon and the muon neutrino have a lepton flavour number $L_\mu = 1$ and the tau and tau neutrino - $L_\tau = 1$. There are twelve additional gauge bosons with spin 1 that are responsible for mediating the interactions between these particles. These bosons are organized as follows: one photon γ for the electromagnetic interaction, three bosons - $W^{\pm}$ and Z^0 - for the weak interaction, and eight gluons g for the strong interaction. Additionally, a scalar boson particle (spin 0), called the Higgs boson H, which is neither a matter particle nor a gauge boson, had been introduced in the theory to explain how some particles, such as the $W^{\pm}$ and Z^0, obtain their masses. Eventhough, it was postulated more than fifty years ago, the discovery of a particle with Higgs like properties and a mass around 126 GeV was announced only in the middle of 2012 by the ATLAS and CMS collaborations at CERN [3]. An update from just a couple of months ago states that this particle resembles more and more the Higgs boson, however additional studies are required to confirm whether it is the predicted boson [3]. Fig. 2.1 summarizes all the known Standard Model particles.

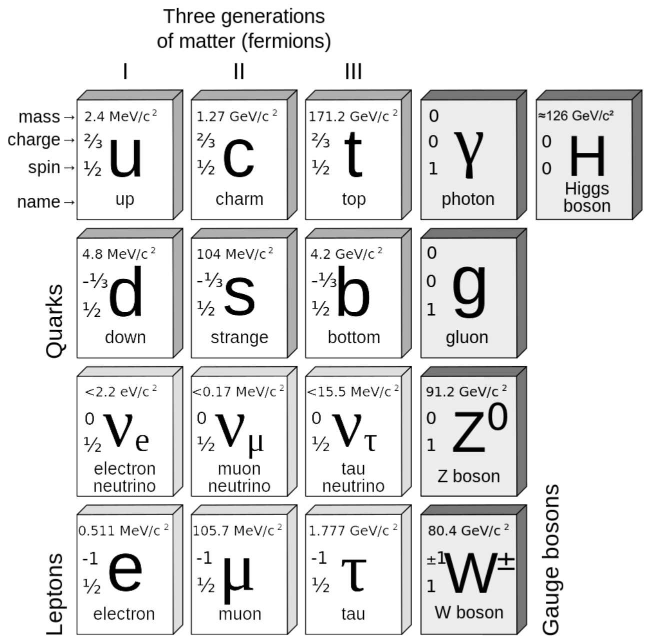

Figure 2.1: Summary of the observed Standard Model particles. Image taken from [4]

Initially, scientists thought that the interactions did not mix members of one lepton or quark generation with members of another generation. However, experimental results on weak decays [5] pointed that this might not be true in the quarks sector and lead first Cabibbo and later Kobayashi and Maskawa to the conclusion that the weak eigenstates with which the quarks participate in the weak interactions are not the same as their mass states [1], but rather they are a superposition of all the mass

[1] The mass states are also the eigenstates of the strong interaction.

states expressed through a 3×3 unitary matrix known as CKM matrix. Hence, in the quark sector there is no analogue to the lepton flavour. On the other hand, the lack of a process like $\mu^+ \rightarrow e^+\gamma$ lead to the conclusion that the muon is a new particle different from the electron [6]. Later experiments proved that also the muon and the electron neutrinos are two distinct particles. Since the neutrinos are massless within the Standard Model framework, there could be no intergeneration mixing in the lepton sector. As a result the muon, which is quite similar to the electron, albeit its higher mass of 105.6 MeV, could only exhibit decays that conserve the lepton flavour number. Its allowed decays and their branching ratios (BR) are summarized in Table 2.1.

Decay Mode	Branching ratio
$\mu^+ \rightarrow e^+\nu_e\bar{\nu}_\mu$	$\sim 100\%$
$\mu^+ \rightarrow e^+\gamma\nu_e\bar{\nu}_\mu$	$1.4(4) \times 10^{-2}$
$\mu^+ \rightarrow e^+e^-e^+\nu_e\bar{\nu}_\mu$	$3.4(4) \times 10^{-5}$

Table 2.1: Summary of Standard Model muon decays which conserve the lepton flavour number. Data taken from [7]

Introducing the neutrino masses

If one abandons the assumption that the neutrinos are massless, then their flavour eigenstates could in general be expressed as a superposition of their mass eigenstates. The three by three unitary matrix which transforms the mass into flavour states is known as the Pontecorvo-Maki-Nakagawa-Sakata (PMNS) matrix. It is parametrized by three mixing angles and a single phase. The probability to observe a neutrino oscillating from one flavour to another is calculated with the help of this matrix and depends on the square of the mass difference between the two neutrino states. Over the last years, several experiments like Super-Kamiokande [8], T2K [9], SNO [10] and Daya Bay [11] have confirmed the existence of neutrino oscillations, proving that the neutrinos are indeed massive. Modifications of the Standard Model include the massive neutrinos and as a result the lepton flavour violating decays of the charged leptons are no longer forbidden.

The $\mu^+ \to e^+e^-e^+$ decay within the Standard Model

An example of a LFV process is the muon decay $\mu^+ \to e^+e^-e^+$. It could be realized within the extended version of the Standard Model via neutrinos oscillating in a loop (see Fig. 2.2).

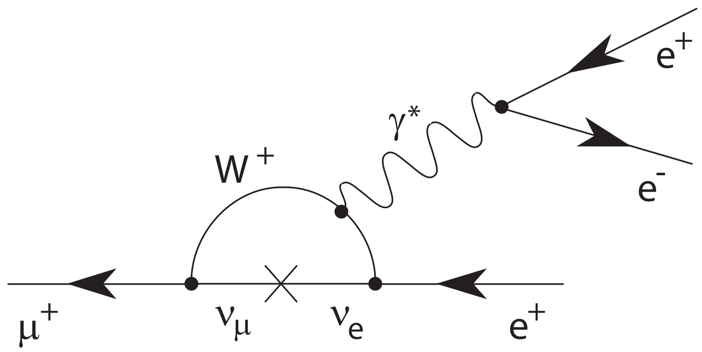

Figure 2.2: Standard Model realization of the $\mu^+ \to e^+e^-e^+$ decay via neutrino oscillation

Despite being allowed, this process is highly suppressed. Its branching ratio is proportional to $\left(\frac{\Delta m_\nu^2}{M_W^2}\right)^2$. The square mass difference of the neutrino, Δm_ν, is estimated to be in the order of $\lesssim 1$ eV^2, while the mass of the weak interaction gauge boson, W, is 80.4 GeV, which leads to a branching fraction BR($\mu^+ \to e^+e^-e^+$)$\lesssim 10^{-50}$. Such sensitivity is far beyond the reach of any present day experiment.

If the photon in the above diagram instead of virtual, was real it would depict a very similar LFV process namely $\mu^+ \to e^+\gamma$. Its branching ratio is a factor of about ~ 100 times $(1/\alpha_{EM})$ higher but it still remains heavily suppressed. Therefore, an observation of any of these decays would be a clear prove for new physics beyond the Standard Model.

2.2 Lepton Flavour Violating Decays beyond the Standard Model

Many theories beyond the Standard Model include naturally processes which do not conserve the lepton flavour number in the neutral or in the charged leptons sectors. Some of them introduce the lepton flavour violation through heavy particles which couple directly to both the electron and the muon. Tree-level diagrams like the one in Fig. 2.3(a) arise in models with extended Higgs sector [12]. The suppression of the $\mu^+ \to e^+e^-e^+$ process in such models is mainly due to the high mass of the mediating particle. Since no such particles are observed, if they exist their mass should be higher than the experimentally accessible scales.

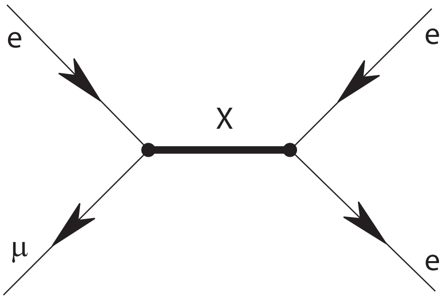

(a) Tree-like diagram arising in theories with extended Higgs sector. The LFV is realized through new mediating particle coupled directly to the muon and the electron.

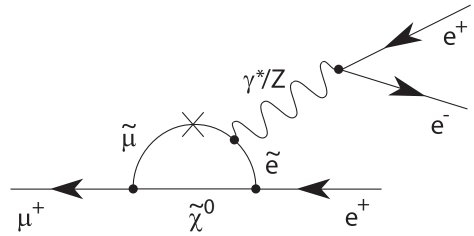

(b) LFV diagram with super-symmetric particles oscillating in a loop.

Figure 2.3: Diagrams of charged LFV processes arising in theories beyond the Standard Model

Another type of diagram that gives rise to lepton flavour violating processes relies on the existence of super-symmetric particles [12] that run in a loop (see Fig. 2.3(b). It is similar to the neutrino oscillation diagram in the Standard Model. However, the new super-symmetric particles could have masses quite different than these of the SM neutrino and W bosons, so the ratio $\left(\frac{\Delta m_\nu^2}{M_W^2}\right)^2$ could eventually be much higher, and thus not suppressing the process so strongly.

Some of these exotic theories predict branching ratio for the $\mu^+ \to e^+e^-e^+$ process just above the experimental sensitivity of the previous measurements BR($\mu^+ \to e^+e^-e^+$)=10^{-12} [2]. However, recent result from the MEG experiment, BR($\mu^+ \to e^+\gamma$)$<5.7\times10^{-13}$ [13], exclude most of the models predicting discoveries just “behind the corner”.

Chapter 3

Experimental Situation in the LFV Searches

With variety of predictions from different theoretical models, the search for LFV in the charged lepton sector have been a topic of interest for many experiments. A summary of the upper limits for different LFV decay modes obtained over the past 60 years is shown in Fig.3.1. After significant improvements thought the years, in the 80s a limit of BR($\mu^+ \to e^+e^-e^+$)<1×10^{-12} [2] was set for the $\mu^+ \to e^+e^-e^+$ decay. In the present section an outline of the results from a few experiments relevant to the $\mu^+ \to e^+e^-e^+$ decay would be given.

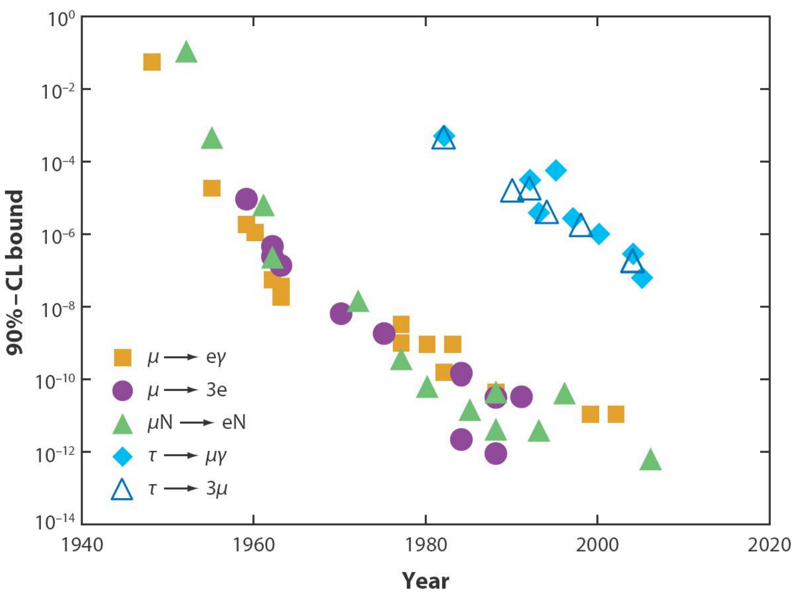

Figure 3.1: Summary of the experimental results from various searches for LFV over the past 60 years. The most recent MEG results [13] are not shown in this plot.

3.1 LFV Search through the Decay $\mu^+ \to e^+e^-e^+$

In the years from 1983 to 1986 the SINDRUM experiment at the Paul Scherrer Institute in Switzerland (PSI) searched for the decay $\mu^+ \to e^+e^-e^+$ with an experimental setup similar to the one proposed in the current Mu3e expeiment. A low energy continuous muon beam was stopped in a hollow double cone target and the resulting decay electrons were detected with multiwire proportional chambers. The detector was placed inside a solenoidal magnetic field of 0.33 T. The sensitivity of the experiment as determined by the resolving capabilities of the detectors was estimated to 5×10^{-14} [2]. However, the limited number of stopped muons allowed only for exclusion of the $\mu^+ \to e^+e^-e^+$ with a branching ratio BR($\mu^+ \to e^+e^-e^+$)<1×10^{-12} at 90% C.L. [2]. The Mu3e experiment aims to improve on the sensitivity in four orders of magnitude compared to the obtained result.

3.2 LFV Search through the Decay $\mu^+ \to e^+\gamma$

The MEG experiment has been running at PSI since 2008 and it has been searching for charged lepton flavour violation through the decay $\mu^+ \to e^+\gamma$. This experiment also takes advantage of a slow continuous muon beam and measures the decay products of muons stopped in a thin target. Drift chambers measure single electron tracks and a liquid xenon calorimeter is used to detect the emitted photons. The dominating background is from accidental coincidence of photons and single positrons and determines maximum sensitivity of 1 in 10^{13}. The results obtained so far from the analysis of the data up to 2012 set a limit of BR($\mu^+ \to e^+\gamma$)<5.7×10^{-13} at 90% C.L. [13]. In case that the dominating effects of LFV are due to dipole couplings, to improve on the 10^{-13} sensitivity of MEG, the Mu3e experiment should be able to reach sensitivity of at least 10^{-15}.

3.3 LFV in Muon Conversion Experiments $\mu^-N \to e^-N$

Another type of experiments that search for lepton flavour violation exploit the conversion of muons in the vicinity of nuclei. The SINDRUM II experiment operated at PSI until 2006 had set the lowest limit of $\mu \to e$ with a BR($\mu Au \to eAu$)<7×10^{-13} at 90% C.L. [14]. The signal event in muon conversion experiments is a monochromatic electron. Background originating from rapidly decaying pions is reduced by the use of a pulsed muon beam. The limits of such experiments are set by the background pions and the normal decays of captured muons. A few experiments are planned for the near future which would try to improve the existing limit measured by SINDRUM II. They include Mu2e at Fermilab [15] and COMET [16, 17] and PRISM [18, 19] at J-PARK and aim for sensitivities of 10^{-16} or better.

The conversion experiments are sensitive to four-fermion coupling interactions similarly to the $\mu^+ \rightarrow e^+e^-e^+$, however they also include light quarks, so in this sense they are complementary to the searches for lepton flavour violation.

3.4 Other Experiments Searching for LFV

Decays of τ leptons could be a source of lepton flavour violation. Different studies are conducted by experiments at B-factories such as CLEO, BaBar and Belle and they set a limit for the branching ratios of 10^{-8} [20] for various τ decay channels. At the LHC, lepton flavour violation could be directly observed in suppersymmetric particles, if such exist, or in decays of the Z boson.

Chapter 4

The Mu3e Experiment

The Mu3e experiment aims to search for the lepton flavour violating decay $\mu^+ \to e^+e^-e^+$ with a sensitivity of one in 10^{16}. A positive result would be a clear sign for physics beyond the Standard Model. On the other hand, if no signal is observed, the $\mu^+ \to e^+e^-e^+$ process will be excluded with a branching ratio of less than 10^{-16} at 90% confidence level (C.L.).

In order to reach the planned sensitivity in an acceptable time scale, the experiment should operate with very high muon rates ($> 2 \times 10^9$ Hz). Additionally, the presence of any background sources should be reduced to levels below 10^{-16}. To achieve these goals a detector with excellent spatial, timing and momentum resolutions should be constructed. Geometrical constrains arising from the positioning of the detector modules, the beam entry and exit points, and the acceptance of the detector modules determine the efficiency of the experiment.

This section introduces the challenges of the experiment by examining the characteristics of the signal decay $\mu^+ \to e^+e^-e^+$. Afterwards, a brief discussion on the various experimental components, such as the accelerator complex, target, detectors and their current design, is presented.

4.1 Kinematics of the $\mu^+ \to e^+e^-e^+$ Decay

Muons decaying at rest will be used in the Mu3e experiment. From momentum conservation, it follows that the signal electrons should have energies adding up to the rest mass of the muon and the vectorial sum of their momenta should vanish.

$$E_{tot} = \left|\sum_{i=1}^{3} E_i\right| = m_\mu c^2 \quad , \qquad |\vec{p}_{tot}| = \left|\sum_{i=1}^{3} \vec{p_i}\right| = 0$$

These conditions are in the core of analysis algorithms to be developed for online events selection. Since, the energy range of the signal electrons is rather wide - from 53 MeV down to 0.5 MeV, to ensure at least 50% acceptance[1] of all events the detector must cover energies starting from 10 MeV.

4.2 Background Sources

Muon decays with final states of three electrons allowed within the SM present an irreducible background to the experiment. An example of such a decay is the process $\mu^+ \to e^+e^-e^+\nu_e\bar{\nu}_\mu$. Additionally, with increasing the intensity of the beam, the number of accidental backgrounds which result from improperly identified events grows.

4.2.1 Irreducible Background Sources

With a branching ratio of 3.4×10^{-5} [7], the decay $\mu^+ \to e^+e^-e^+\nu_e\bar{\nu}_\mu$, contributes most seriously to the background of the experiment. The produced particles originate from the same vertex and they are emitted simultaneously, so track reconstruction and time coincidence techniques cannot be used to isolate this process from the signal $\mu^+ \to e^+e^-e^+$ decay. One could only rely on energy and momentum conservation to distinguish between the two processes. The neutrinos do not interact with matter[2], so the momentum they carry away can only be measured indirectly from the missing momentum of the electrons that are detected. Because of the small neutrino masses, the energy spectrum of the electrons from the $\mu^+ \to e^+e^-e^+\nu_e\bar{\nu}_\mu$ decay has a tail on the right similar to that of the beta decay. Fig. 4.1 shows the branching ratio for the $\mu^+ \to e^+e^-e^+\nu_e\bar{\nu}_\mu$ as a function of the missing neutrino energy. In one of 10^{15} cases, for example, the neutrinos have a momentum of 2 MeV. Suppose that the detector has an energy resolution of 5 MeV, then there is no way to distinguish a background event from a signal event since the reconstructed energy of the electrons from both processes ($\mu^+ \to e^+e^-e^+$ and $\mu^+ \to e^+e^-e^+\nu_e\bar{\nu}_\mu$) would be the same within the precision of the measurement. To exclude the possibility of having non-signal events for a sensitivity of 1 in 10^{16}, the detector should be able to determine the electrons

[1] Various models predict different energy distributions of the outgoing electrons, so the acceptance level is based on the results of all models and and is chosen such that for any model at least 50% of the events would fall in the accessible range of the detector.

[2] They could in theory interact within the detector but the cross-section is in the order of 10^{-44}, so it could be accepted that they cannot be detected.

energy with a resolution of at least 1 MeV.

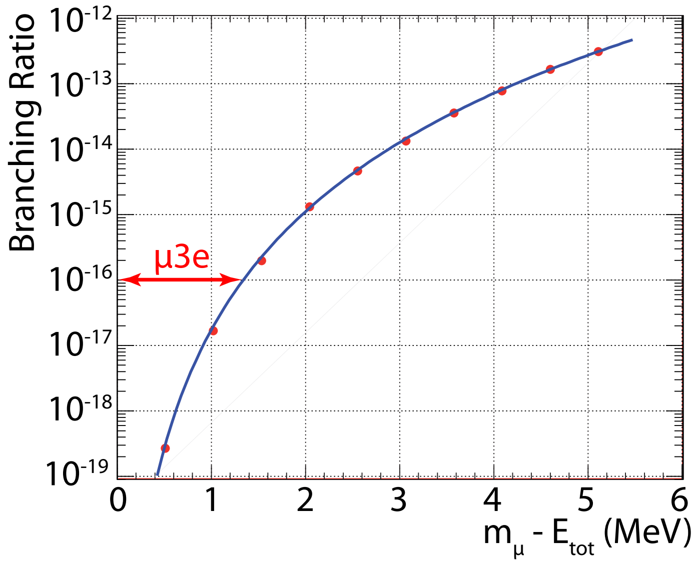

Figure 4.1: Branching ratio of the $\mu^+ \to e^+e^-e^+\nu_e\bar{\nu}_\mu$ decay as a function of the missing neutrino energy. The resolution needed to discriminate this process from the $\mu^+ \to e^+e^-e^+$ should be better than 1 MeV

4.2.2 Accidental Backgrounds

In the accidental or combinatorial backgrounds, the electron and the two positrons have energies consistent with these of the signal event, however, they emerge from different processes. For instance, one positron could be produced in the ordinary Michael decay ($\mu^+ \to e^+\nu_e\bar{\nu}_\mu$) and another positron and an electron could result from an internal conversion (Fig. 4.2(a)). The probability for internal conversion is lower when the material of the detector is minimized. The positrons of two Michael decays and an electron might also mimic the $\mu^+ \to e^+e^-e^+$ event. (see Fig. 4.2(b)). The electron could come from a photon conversion, Bhabha scattering, or it could be a misidentified recurling positron.

Although the particles' energies add up to the muon mass, such events are not coincident in time and the particles involved in them originate from different space points. Good vertex reconstruction and time information are the only means by which one could separate these accidental backgrounds from the signal events.

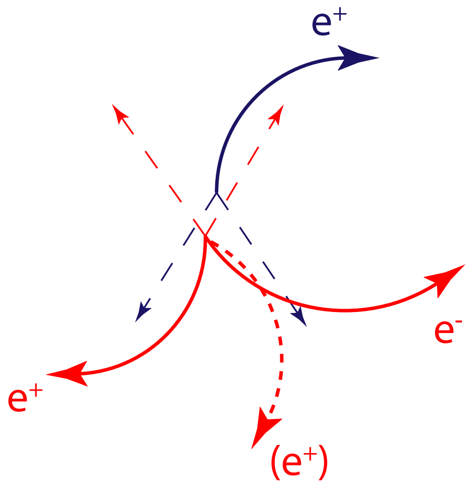

(a) A positron from a Michael decay and positron and an electron produced in an internal conversion ($\mu^+ \to e^+e^-e^+\nu_e\bar{\nu}_\mu$)

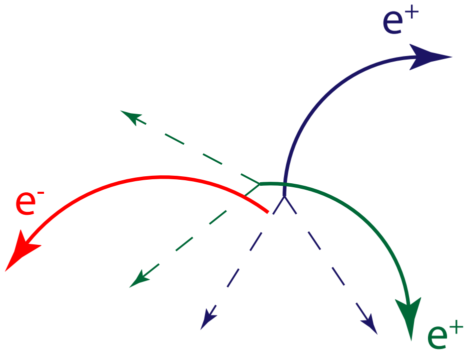

(b) Two positrons from Michael decays and an electron

Figure 4.2: Combinatorial background events mimicking the signal decay

4.3 Muon Beam

To achieve the desired sensitivity of one in 10^{16} muon decays in reasonable time scale, the Mu3e experiment requires beam intensity in the order of more than 10^9 muons per second. There are several facilities in the world which deliver high intensity muon beams. The PSI in Switzerland is, however, the one providing the highest continuous rates (DC). At present the intensity of the muon beam is in the order of 2×10^8. Such rate is sufficient for the first phase of the experiment.

An accelerated proton beam of energy 590 MeV/c and intensity of 2.3 mA impinges on a rotating carbon target and produces pions. The pions then decay at rest close to the surface of the target with one of the products being mono-energetic muons. Currently, the beamline $\pi E5$ at PSI delivers this intensive beam to the MEG experiment (see Fig. 4.3). The projects plans are to have the beamline extended so that it could be used by the Mu3e experiment as well (see Fig. 4.4).

For the second phase of the Mu3e experiment the intensity of the beam needs to be increased with one order of magnitude up to 2×10^9 Hz. Stopping the protons at the neutron spallation source SINQ provides large number of muons. A research is ongoing at PSI on the possibility of using this target to generate more intensive muon beam.

Figure 4.3: Partial scheme of the PSI accelerator complex

4.4 Stopping Target

The analysis of the Mu3e experiment relies on the fact that the muons decay at rest, so the stopping target is a significant part of the design. To provide good conditions for vertex reconstruction, the target must be constructed such that the muons stop uniformly over a large area. Furthermore, it must be build with as little material as possible, to reduce the scattering probability for the decay electrons. The latest design ideas suggest the use of a hollow aluminium double cone target with a thickness of 30µm in the front part and 80µm in the back part. The length and the radius of the cone are 100mm and 10mm, respectively.

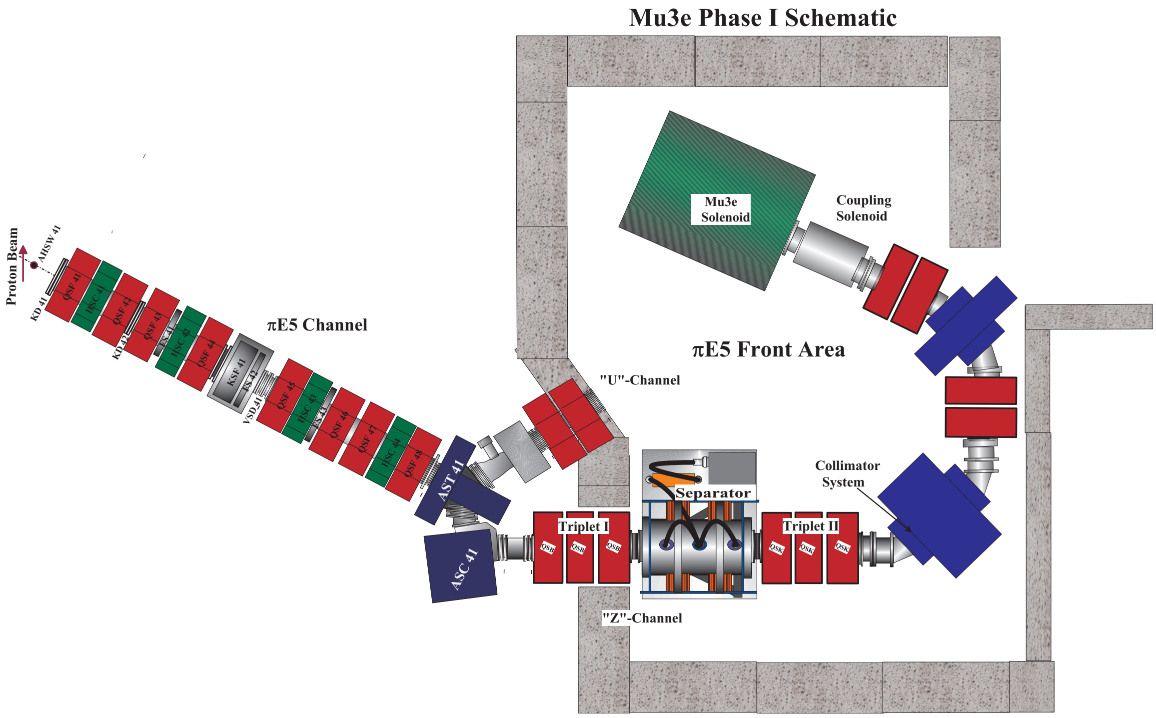

Figure 4.4: Scheme of the beam line for the first stage of the Mu3e experiment

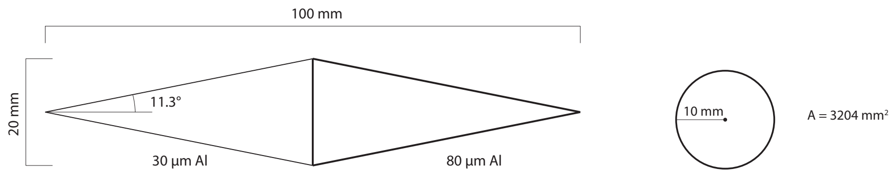

(a) (b)

Figure 4.5: Schematic view of the target design

4.5 Mu3e Detector

A schematic drawing of the Mu3e detector is presented in Fig. 4.6. The detector is cylindrical in shape and consist of several layers of sub-detector units. It is divided into a central part, positioned around the target, and outer parts on the two sides, called recurl stations (one or two pairs). The central part contains an inner and an outer pixel layers which compose part of the tracker module. Between them, there is a layer of staggered scintillating fibres which provide timing information needed for track reconstruction. Additional pixel layers and scintillating tiles are envisaged for the recurl stations. To identify positrons and electrons and determine their momenta, the whole detector is placed inside a homogeneous magnetic field of strength about 1 T.

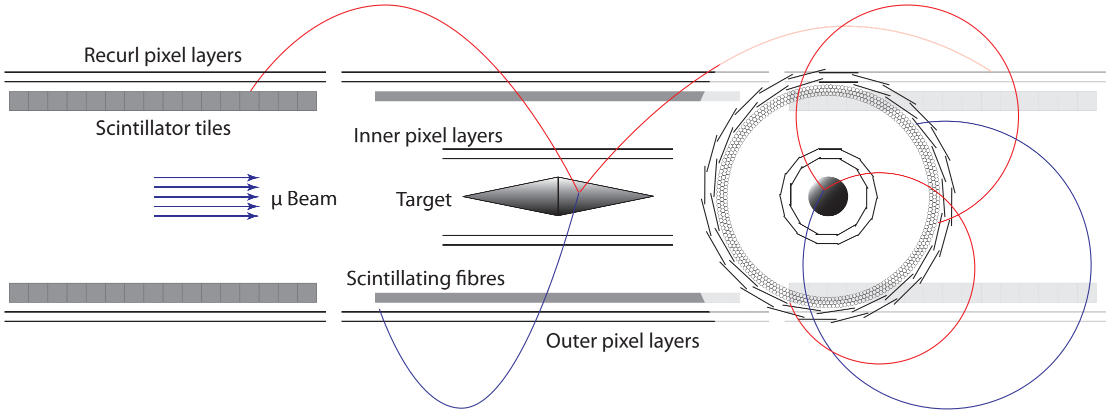

Figure 4.6: The central part of the detector together with one pair of recurl stations. The blue and red curves are simulated tracks of a signal event - two positrons and an electron. On the right is displayed the cross-sectional view of the detector.

4.5.1 Tracker Module

The tracker module provides information to reconstruct the paths of the electrons moving inside the magnetic field and measure their momentum. When electrons traverse a given material they interact electromagnetically with the atoms of the medium. For thin materials, the multiple interactions lead to a change in the trajectory of an electron with a deflection angle inversely proportional to the initial electron momentum and increasing with the thickness of the medium [21]. A detector with the least possible material [3] should, therefore, be used. Moreover, the detector needs to be highly segmented to ensure good position resolution. A novel technology of high voltage monolithic active pixel sensors (HV-MAPS) [22] satisfies the requirements of the experiment. The analogue and digital electronics are built directly on the sensor, eliminating the need of having additional readout chips inside the active area of the detector. Its thickness could be reduced to less that 50μm without deteriorating the signal quality, which corresponds to radiation lengths in the order of less than 0.1%. Such values are comparable to tracking systems based on gaseous detector.

HV-MAPS Fig. 4.7 presents a schematic of a HV-MAPS detector and a diagram of its readout scheme. The pixel electronics is placed inside a deep N-well. When a particle traverse the depletion region it creates charged carriers which move though

[3] in terms of radiation lengths it is required to be of thickness $X/X_0 \approx 0.1\%$

strong electric field to the collection electrodes. Bias voltage in the order of 50 V ensures short drift time of the particles and leads to faster signals.

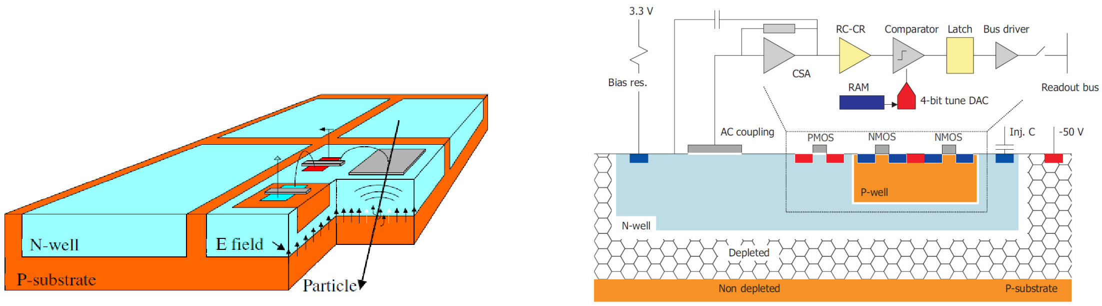

(a) (b)

Figure 4.7: Schematic of HV-MAPS cell and readout (figure taken from [22])

Tracker design Four layers of HV-MAPS detectors form the central part of the tracker. The inner two pixel layers are placed close to the target at a distance of 2 cm and 3 cm respectively, as shown in Fig. 4.6. They cover a length of 12 cm and, besides participating in the momentum measurements, their main purpose is to facilitate the vertex reconstruction. The outer layers are also arranged in a cylindrical shape with radii of 7.3 cm and 8.5 cm and a length of 36 cm. Four additional sets of outer layers in the recurl stations measure electrons with high momentum and result in momentum resolution of RMS(p) = 0.28 MeV/c [1]. For the first stage of the experiment only two of the recurl stations will be used, and the other two will be added in the second phase. The final length of the detector will be around 2 m and it will be composed of approximately 280 million pixel cells with dimensions $80 \times 80 \mu m$.

4.5.2 Scintillating Fibre Tracker/Time-of-Flight Detector

Motivation

The readout of the data will be done in 50 ns frames. At a rate of 2×10^9 muons stopped per second the number of tracks in the detector reaches 100 per frame. A simulation of the detector occupancy for one time frame is shown in Fig. 4.8(a). The time resolution of the silicon pixels is in the order of the frame duration and the expected average distance between two vertices is less than 1 mm [1]. Therefore, to distinguish close tracks of two different events a time resolution better than 1 ns is required (100 tracks in 50 ns, continuous muon current $\Rightarrow$ time resolution = 0.5 ns). Fig. 4.8(b) demonstrates the effect on track reconstruction if time information is available. To suppress the accidental backgrounds discussed earlier it is essential to properly identify the separate tracks.

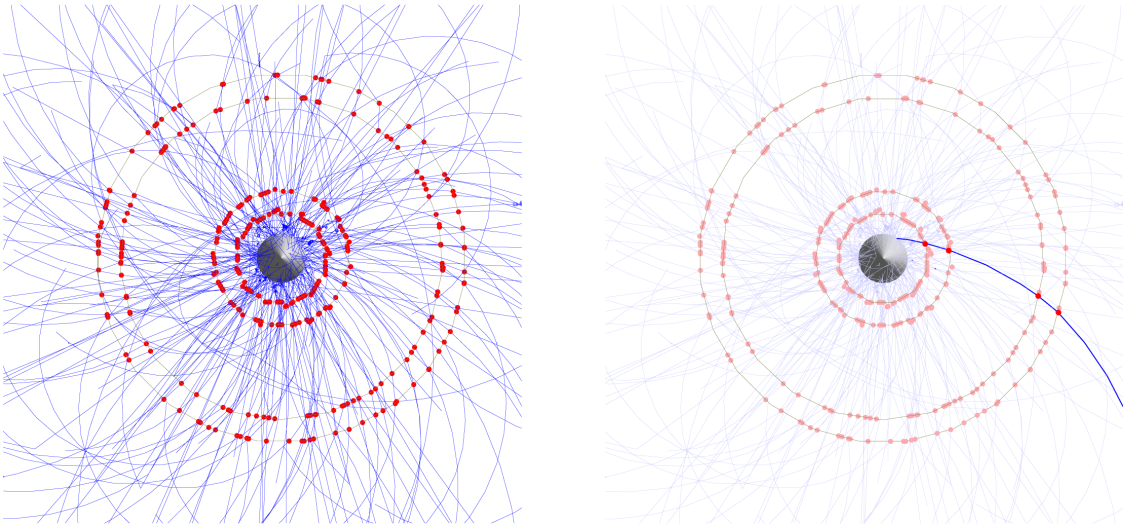

(a) (b)

Figure 4.8: Simulation of events per one readout frame of 50ns. There will be around 100 tracks in one data frame as shown on the left. A timing module with high resolution is required to properly identify the single tracks. The effect of having less than 1 ns resolution is presented on the right. Figures from [23].

Time-of-flight system

A scintillating fibre (Sci-Fi) hodoscope with a length of 36 cm and a radius of 6 cm is proposed in response to the above requirements. It will be placed between the inner and outer layers of the silicon tracker. To complement the fibres tracker there will be four other cylindrical detectors with a length of 36 cm and a radius 12 cm, built of scintillating tiles and positioned on the inner side of the recurl pixel layers (see Fig. 4.9). The photons of both systems will be read by silicon photomultiplier (SiPM) sensors. The expected time resolution of the Sci-Fi hodoscope is a few hundred picoseconds, while that of the tile detector is better than 100 ps.

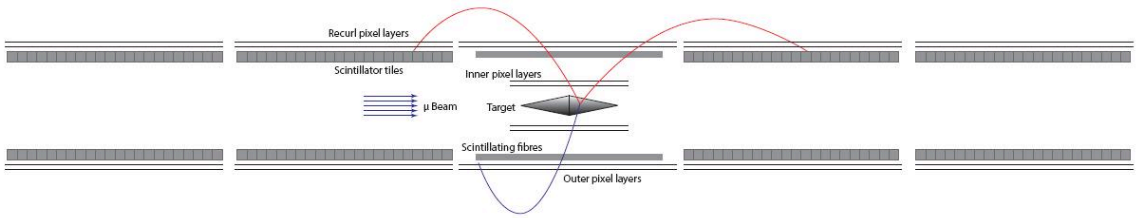

Figure 4.9: The central part of the detector together with two pairs of recurl stations.

4.5.3 Fibre Detector

The requirements for the Sci-Fi time-of-flight detector are rather though because of its position between the layers of the pixel tracker. A compromise should be found between two opposing requirements. On one side, the thickness of the fibres should be kept low to reduce the effects of multiple scattering influencing the track reconstruction. On the other hand, to achieve the desired time resolution of a few hundred picoseconds and to ensure high efficiency the module needs more material. A solution is proposed through the use of plastic scintillating fibres with diameter of 250 μm staggered as tightly as possible in ribbons. Three to five layers of fibres result in about a millimetre of thickness. The width of a single ribbon is 16 mm and its length is 36 cm. Twenty-four ribbons arranged in a cylindrical structure as the one shown in Fig. 4.10 will form the active area of the central time-of-flight detector. The total number of fibres in the case of three layers per ribbon amounts to 4600, and if there are five layers it will reach nearly 7500. The large number of fibres is necessary to provide information on the position where the electrons cross in order to facilitate the track reconstruction. The light produced in the fibres is detected by SiPM sensors mounted at both ends of the ribbons. These devices have numerous advantages over conventional photomultipliers: compact size (∼few mm), high gain factor ($\sim 10^6$), insensitivity to magnetic fields. Additionally, the SiPMs could be operated at very high rates. Their photodetection efficiency (P.D.E) is similar to the quantum efficiency of the photomultiplier tubes and is in the order of 20-25%.

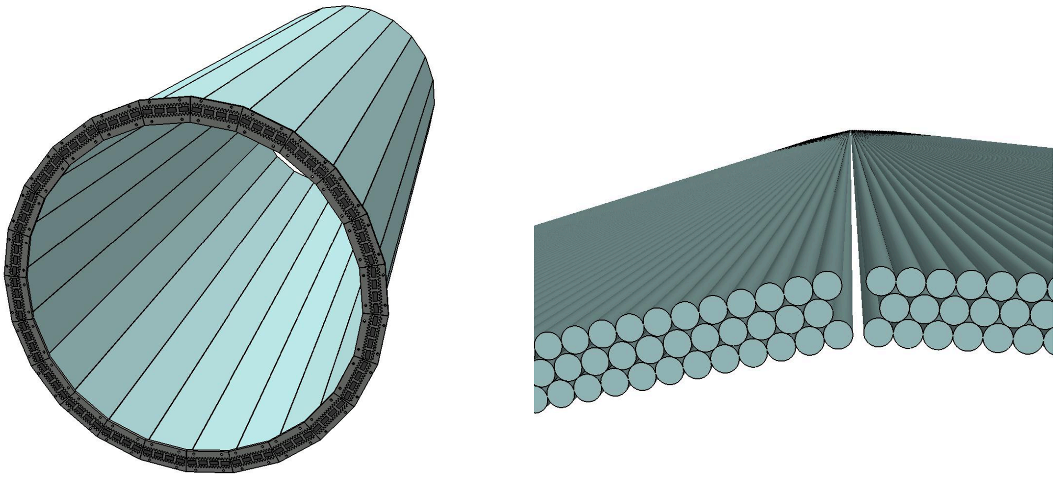

(a) (b)

Figure 4.10: Concept of the Sci-Fi time-of-flight module. Figures taken from [1]

Fibres readout options

Depending on the occupancy of the fibres, two possible configurations of SiPMs are considered for the readout. One of the options utilizes SiPM arrays organized in columns with active width of 250μm. Each array covers the cross-section of one ribbon and outputs a combined signal from several neighbouring fibres. In a second scenario, the individual fibres are readout separately.

SiPM arrays

The Japanese company Hamamatsu offers monolithic SiPM arrays with 64 channels and a single pixel size of $50 \times 50\mu m^2$ [24] (see Fig. 4.11(a)). The dimensions of one array are 16mm×1mm (active area) and they match exactly the cross-section of one ribbon. To increase the light collection the SiPM detectors are glued directly to the polished ribbons. The total number of readout channels with such arrays for both sides of all ribbons is $24 \times 2 \times 64 = 3072$. When a particle crosses a fibre it triggers the detectors at both ends, so the number of channel necessary to estimate the occupancy of the detector is half of all the channels. Some of the possible ways for a particle to traverse a ribbon are illustrated in Fig. 4.11(b). For the minimal case of three layers, one particle might cause up to 2-3 channels in a SiPM array to fire. Since the particles are in a magnetic field most of the time they traverse the ribbon at an angle as shown by the third track in Fig. 4.11(b). With 2×10^9 decays per second and 1500 available channels the system must be read at rates of 5 MHz ($\frac{2\times10^9}{1500}$ provided that the number of dark-counts is reduced to zero). Additionally, the spreading of a single event over several channels requires the design of clustering algorithms to extract timing and position information.

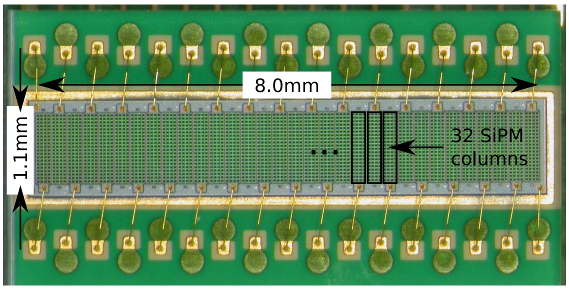

(a) A photo of a 32-channel SiPM produced by Hamamatsu (figure taken from [25]

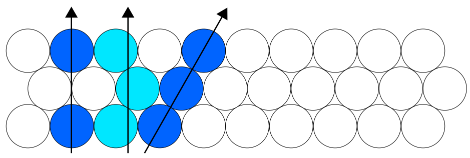

(b) Example trajectories of an electron crossing three-layer ribbon

Figure 4.11: A SiPM device and a cross-section of a ribbon considered for the column by column readout of the Sci-Fi module

Single fibre readout An alternative design that relaxes the high demands of 5 MHz readout is based on a single fibre readout. With a total number of 9000 channels in the three-layer configuration, the reduction factor is 3 leading to less than 2 MHz readout rate. Handling such rates is feasible with present day electronics [26].The problems such readout rises are related to the light propagation in the fibres and more specifically to the light exiting the fibres. Simulation studies show that for multi-cladding fibres such as the ones considered for this experiment, the scintillating photons travel predominantly in the cladding (see Fig. 4.12).

Moreover, if the end points of the fibres are in contact with air, the light spreads in a cone at 45^o (Snelius's law). To collect all the light from a given fibre a photon detector with active area larger than that of the fibre should be used. The idea is to have at least 100 μm of extra space per fibre to capture all the photons and also to accommodate any small misalignments of the fibres. Ideally, SiPM detector arrays with pixels grouped into clusters of size about 400×400 μm^2 and separated by inactive area of 50-100 μm should be produced and coupled through plastic connectors with the same mask to the fibres. The inactive area would reduce the optical cross-talk caused by the light spreading out of the fibres. The disadvantage of such design is that the size doubles in the already tight configuration of the whole detector. There should be also a transition region of about 2-3 cm for the fibres from the ribbons to enter the connecting sockets. If the SiPMs cannot be coupled to the fibres through such sockets, options with optical fibres leading the light out of the detector sensitive

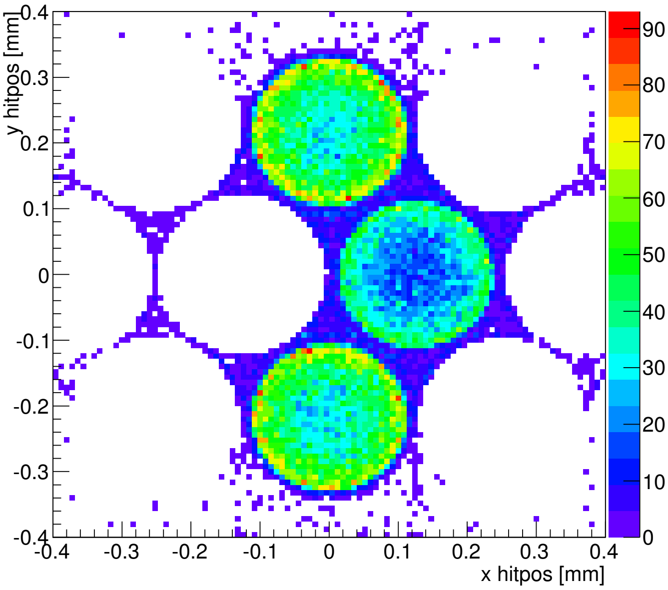

Figure 4.12: Simulation of scintillating light propagating through the fibres. Most of the photons travel in the cladding. Figure provided by Roman Gredig.

area are also considered. They are, however, undesirable and lead to unnecessary complications of the system. Furthermore, the light at the point with optical contacts between different media and even fewer photons reach the SiPM detectors.

The first prototype ribbons with attached connectors for the two types of readout were constructed in the scope of this master thesis. More details on the construction process, including some pictures, are given in the next chapters.

4.5.4 Tile Detector

The tile detector has four components mounted on the inner side of the four recurl stations. It is optimized for a high timing resolution of less than 100 ps. The detector is composed of scintillating plastic tiles with size of $7.5 \times 7.5 \times 5$ mm^3 arranged on a cylinder with a radius of 6 cm. (see Fig 4.13). When a particle hits the tiles it produces a lot of photons, a prerequisite for the desired timing resolutions [4]. Each tile is read by a directly coupled to it SiPM device. Tests carried out by other groups with $1 \times 1 \times 1$ cm^3 NE110 scintillating tiles and 3×3 mm^2 Hamamatsu detectors show promising results of 45 ps time resolution [1].

[4] The time resolution improves with the square root of the detected photons

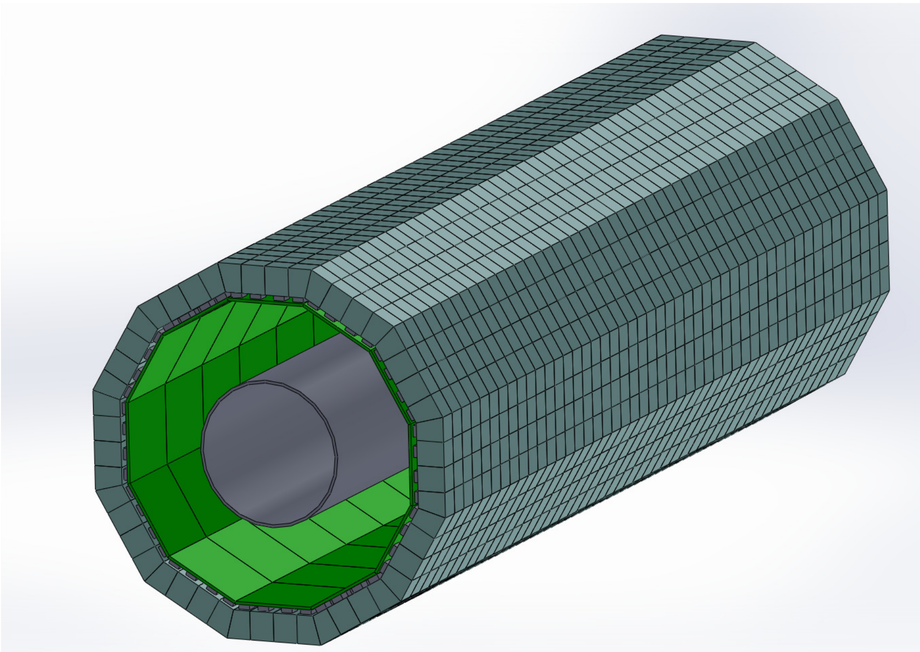

Figure 4.13: Concept design of the tile detector [1]

Chapter 5

Scintillating Fibre Tracker/Time-of-Flight Detector

5.1 Scintillating Fibres

Scintillating materials convert energy deposited in them by a charged particle e.g. an electron, into visible light photons. The intensity of the light produced in a scintillator depends on the energy transferred to it by a passing particle. Two classes of scintillating materials exist depending on their content - organic and inorganic. The principles of light production in both of them are, however, slightly different and details could be found in [27]. In the present work we briefly outline the scintillating mechanism for organic materials, since we plan to use plastic scintillating fibres for the Mu3e experiment. Their advantages include short decay time ($\tau \sim 2-3$ ns) and low effective atomic number. The low density of plastics (contrary to glass for example) is significant for minimizing the electrons scattering in the SciFi hodoscope.

Scintillating light

Plastic scintillators have a molecular structure with a complex electron energy spectrum. Scintillating light in them is produced via transitions of electrons from excited to the ground states of the molecules. When a molecule absorbs energy, its electrons excite to one of a number of possible states called singlet states and labelled S_0, S_1, S_2... in Fig. 5.1. Each of these states is fragmented into several vibrational states, denoted with a second lower index, which have smaller energy spacing. If an electron is excited to a higher energy state (vibrational or singlet) it quickly de-excites to the S_{10} state through an internal conversion and without emitting any light. The scintillating light is generated during the transition from the S_{10} state to one of the S_0 states. The fact that the energy spectrum is so segmented prevents further absorption of the scintillating photons, hence the material is transparent for its own scintillating light. The states labelled with T are called triplet states and they have much longer life-time compared to the singlet states. The process of light emission through transitions in the triplet states is significantly slower and is known as phosphorescence.

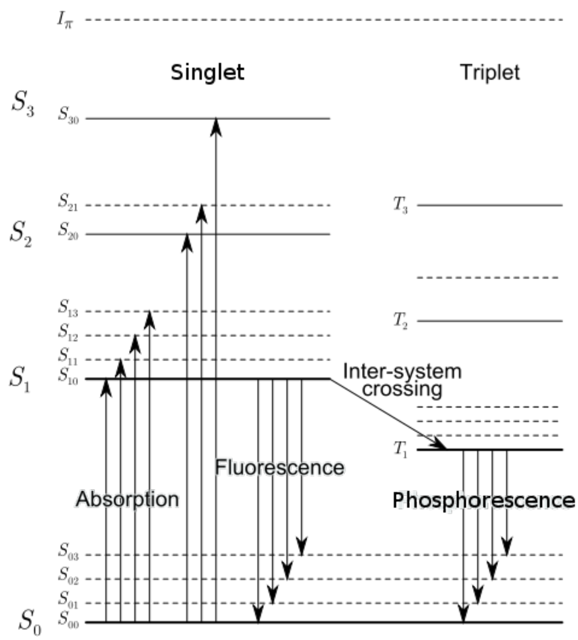

Figure 5.1: Electron energy levels of an organic molecule. S_0 is the ground state. S_1, S_2, S_3 are excited singlet states. T_1, T_2, T_3 are excited triplet states. The vibrational levels are labelled $S_{00}, S_{01}, S_{10}, S_{11}$ etc. Transitions among the singlet states result in scintillating light. The figure is taken from [27]

KURARAY scintillating fibres

The plastic scintillating fibres SM81, produced by the Japanese company KURARAY [28], are characterized by a short decay time of 2.4 ns and a long attenuation length of 3 m. Their properties match the Mu3e timing hodoscope requirements. The light emission spectrum of the SM81 fibres peaks at 440 nm (see Fig. 5.2(a)). A SiPM device sensitive to this wavelength is produced by another Japanese company, namely Hamamatsu photonics (see Fig. 5.2).

We intend to use scintillating fibres with a diameter of only 250 μm, so it is essential to optimize the intensity of light reaching the photon detector. Besides the

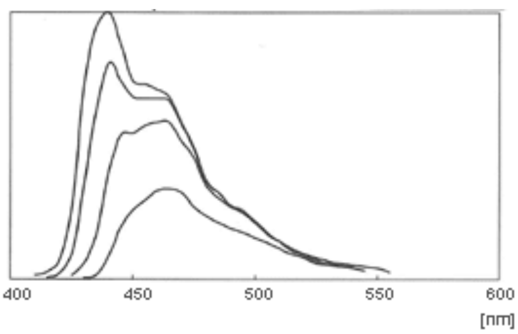

(a) Light emission spectrum of Kuraray SM81 fibres (figure taken from [28]

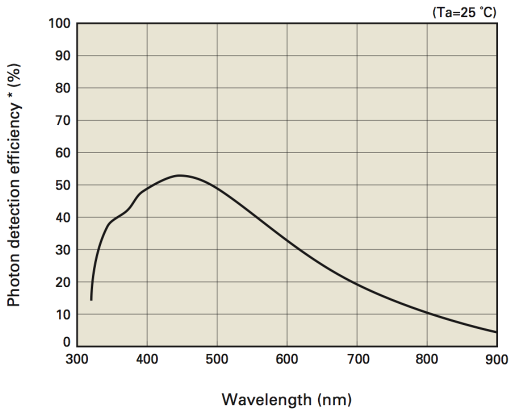

(b) Photon detection efficiency of Hamamatsu MPPC devices (figure taken from [24]

Figure 5.2: The wavelength absorption spectrum of the Hamamatsu MPPC devices used in this work matches the light emission spectra of the Kuraray SM81 fibres

properties of the material like photon yield per deposited energy, density of the material, etc., one could improve on the light collection by using multi-cladding instead of single cladding over the scintillating core of the fibres. Fig. 5.3 illustrates light trapping in a double cladding of fibres produced by KURARY. Due to the second refractive layer, photons emitted at an angle of 26.7 degrees with respect to the longitudinal direction of the fibre remain trapped inside. For a single-clad fibre this angle is only 20.4 degrees. As a result, the trapping efficiency is 5.4% for double cladding and just 3.1% for single cladding.

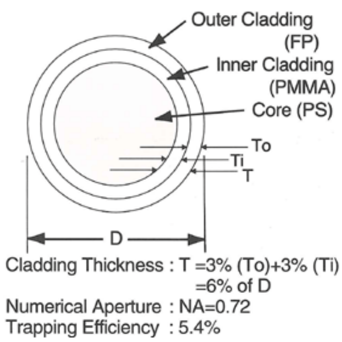

(a)

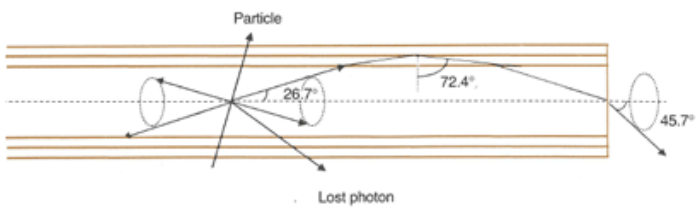

(b)

Figure 5.3: Multicladding of scintillating fibres by Kuraray [28]

An estimate of the number of photons produced by a single electron into a 250 μm multi-clad fibre, which propagate in the fibre gives [27]:

$$10 \times 200 \times 0.25 \times \frac{1 - \cos(26.7^o)}{2} \approx 26 \text{ photons}$$

The first number is the average number of photons yield per 1 keV deposited energy; 200 keV is an estimate of the energy loss per 1 mm of scinitillator by a minimum ionizing particle e.g. an electron with energy of a few MeV ; 0.25 - the maximum thickness of the fibre expresseed in mm; and the last term reflects the fraction of all the photons that stay trapped within the fibre due to internal reflection of the cladding layer, i.e. the trapping efficiency of the fibre. For comparison in a fibre with single-cladding the number of photons is 15.

5.2 Silicon Photon Counter

A SiPM is a photon detector composed of multiple avalanche photodiodes operated in a limited Geiger mode (see Fig. 5.4). It has been proposed approximately two decades ago and since then has undergone significant improvements [29] . It has many advantages e.g. compact size, low operational voltage and insensitivity to external magnetic fields, which make it a strong competitor to the conventional photomultiplier tubes used in most present day applications requiring counting of single photons.

5.2.1 Principle of Operation

Each avalanche photodiode represents a pixel of the SiPM array. The pixels are joined together on a common substrate and they are under high reverse bias. When a photon hits one of the pixels there is a certain probability ($\sim 20\%$, also know as photo detection efficiency, PDE) that it would create an electron-hole pair. Since the diode is biased, the electron accelerates in the high electric field and generates an avalanche discharge. Due to the small thickness of the pixel, a few μm, the discharge time is less than 1 ns resulting in very fast SiPM devices. The number of charge carriers at the collection point, i.e. the gain, is about $10^5 - 10^6$. A quenching resistor in the form of a film over the pixel, stops the avalanche when the currents through the device become too high. Irrespectively of the number of incident photons on one pixel, it produces the same amount of discharge. In this sense, the single pixels are binary devices: they only provide information whether at least one photon was detected or not, but not if there were more.

In a SiPM device the number of pixels could vary from hundreds to thousands. The output signal is equal to the analogue sum of the signals from all the individual

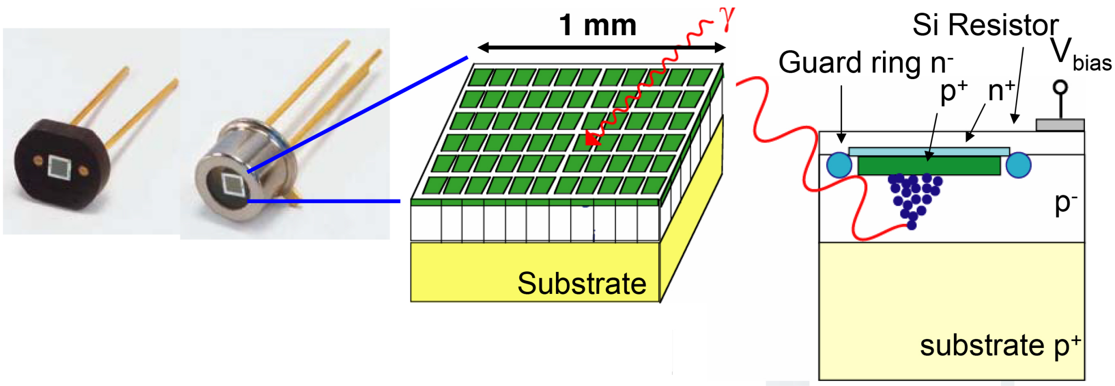

Figure 5.4: Operational principle of a SiPM device. Figure taken from [30]

pixels in which an avalanche was produced. It is proportional to the intensity of the incident light if the number of photons hitting the device is much smaller than the number of pixels. If there are too many photons the probability of having more than one photon hitting a single pixel increases and the detector looses its proportionality.

5.2.2 Performance of Hamamatsu MPPCs

All devices used in this work are Hamamtsu S10362-33-050C model. Each detector has 3600 pixels over an active area of 3×3 mm^2. The size of a single pixel is 50×50 μm^2. The following paragraph outlines the main characteristics of this devices as measured for this thesis.

I-V curves

The multi pixel photon counters exhibit current voltage relations similar to those of a diode. A quad bias supply by Ortec, model 710, provides information about both the voltage over a connected device and the current flowing through it. Such a module was used to derive the I-V curves presented in Fig. 5.5. The SiPM devices behave to good degree like diodes [1] when connected in an electrical circuit. Their breakdown voltage, however, cannot be determined directly from the slope of the I-V curves, as in the case of ideal diodes. The SiPM sensors have rather wide and smoothly changing voltage range available for adjustment of the operational voltages. The breakdown voltage can be extracted from the amplitude of the signals and the results are presented in the "Gain" paragraph.

[1] From now on whenever a diode is mentioned in the text it means the SiPM device unless noted otherwise.

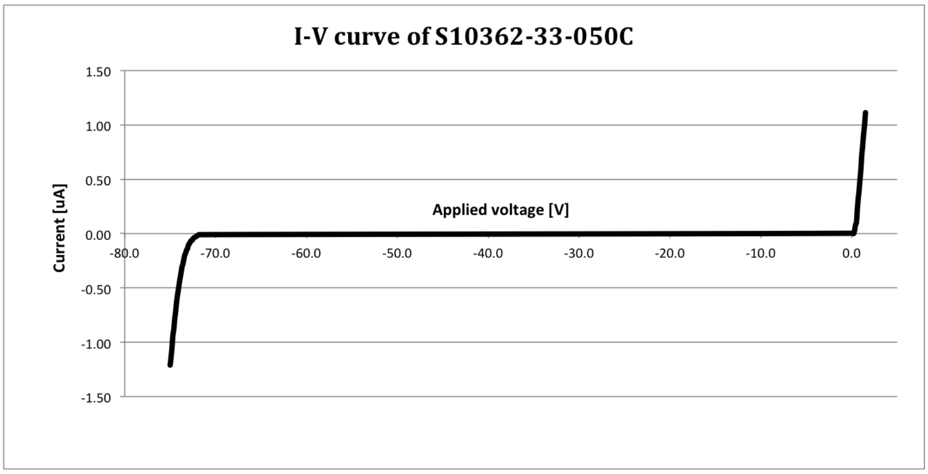

(a)

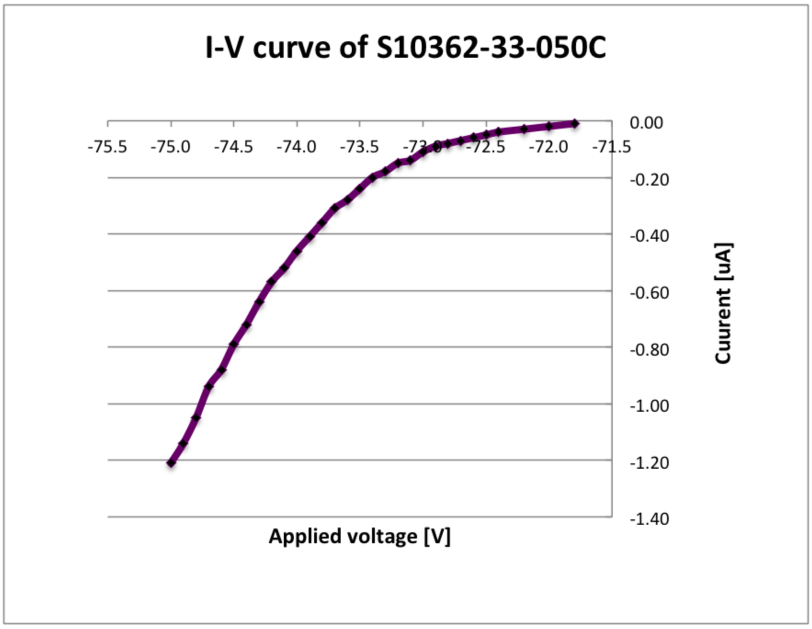

(b)

Figure 5.5: IV curve of S10362-33-050C MPPC as measured with the Ortec 710 high voltage unit

Signal shape

A single pixel yields approximately 10^6 electrons over a time of $\sim$1 ns whenever a discharge occurs. The amplitude of an output signal over a 50 Ω load is in the order of a few mV. Such signal could be transmitted through cables without deteriorating significantly. However, for timing and amplitude measurements with electronic modules like the LeCroy 825E discriminator and the LeCroy 2249A and 2228A modules used in this work, it still needs to be amplified. The electrical engineers group at the DPNC developed a transistor based amplification board with an integrated input for the high voltage supply of the diode. The waveform of the SiPM signals after passing the amplification stage have a rise time of 1.2 ns and a fall time of less than 20 ns for signal of one fired pixel (see Fig: 5.6). The short rise time is crucial for any timing measurements since the time jitter from the discriminator is less when the slope of the signal is more steep. Additionally, in high rates experiments as the future Mu3e, the signal should be short to reduce pile-up events.

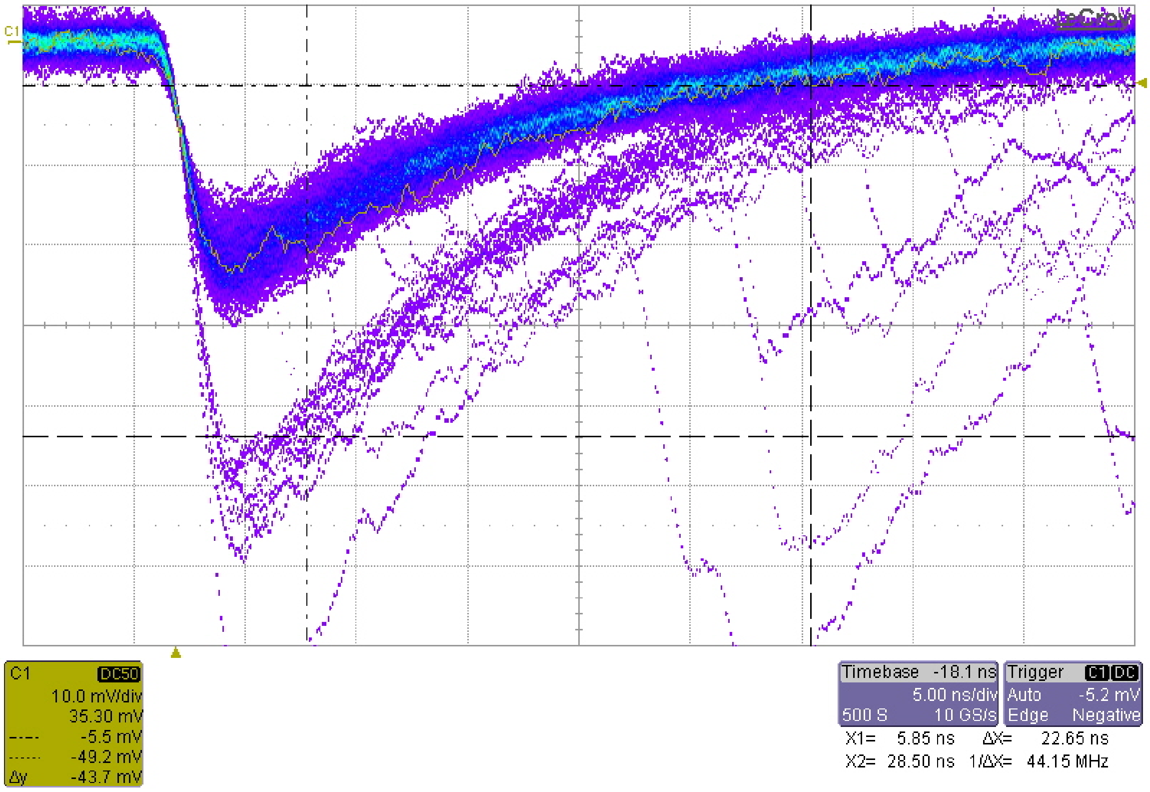

Figure 5.6: Signal shape of a S10362-33-050C device after amplification with the $DPNC286\_07A$ board

Gain

Fig. 5.7 represents the pulse-height spectrum of one of the SiPMs when illuminated by low intensity light source, in this case the photons come from a scintillator coupled to the device and irradiated by a ^{90}Sr source. The persistence time of the display was set to 10 ns. Each cluster of amplitudes corresponds to a fixed number of pixels that produced a signal. The signals are equidistant and well separated which is a direct evidence for the gain uniformity across different pixels. Using the distance between two photo-electron peaks, one could also study the dependence of the gain on the applied voltage over the diode. The graph in Fig. 5.8 shows the results for a range of 2 V over the breakdown voltage.

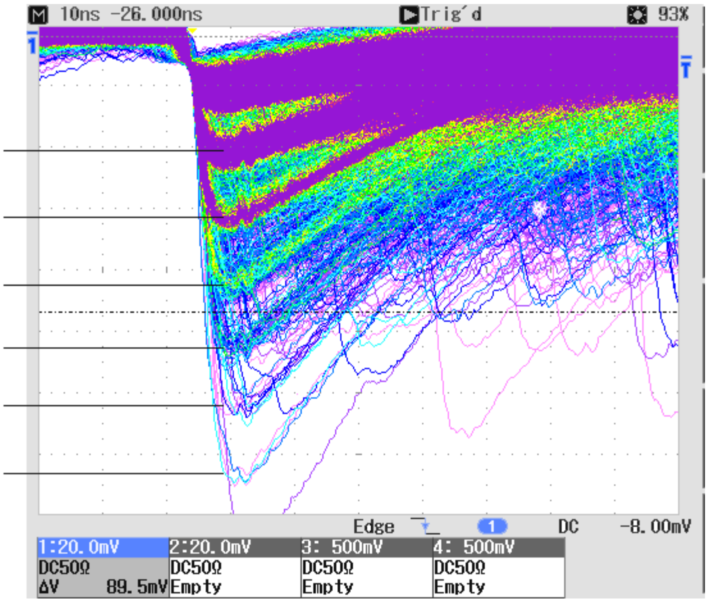

Figure 5.7: Pulse height spectrum of a SiPM device illuminated by scintillating light. A radioactive source ^{90}Sr generates photons in scintillating fibres coupled with the SiPM detector

The amplitude of the signals is proportional to the gain of the device. The gain, on the other hand, is linearly dependent on the applied overvoltage V_{ov}. The overvolatge is defined as the difference between the applied reverse bias voltage V and the breakdown voltage V_{bd}. So, the breakdown voltage could be found by taking the amplitude of the first photoelectron peak for different values of the applied voltage and extrapolating by straight line to the point where the amplitude becomes zero. For the tested device S10362-33-050C a value of 71.4 was obtained. It is consistent with the value determined by observing on an oscilloscope when the device breaks down.

Dark counts and crosstalk

Dark counts are called the events when a discharge is generated in the absence of any incident photons. SiPMs exhibit relatively high dark count rates due the high probability of thermal electrons triggering a discharge in a pixel. Dark count signals

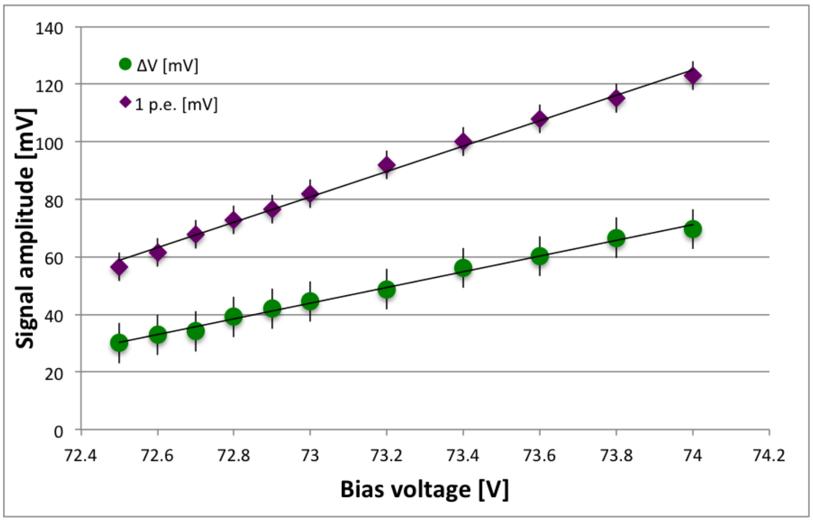

Figure 5.8: Gain of a SiPM device depending on the applied bias voltage. The green dots represent the difference between the amplitudes of the SiPM signals when one and two pixels fired. The purple squares correspond to the signal amplitude when one pixel fired.

are indistinguishable from real signals. The dark counts rate could be evaluated by setting a threshold at half the amplitude of the first photo-electron ("0.5 p.e.") and counting the number of events in conditions with no light.

Pixels crosstalk or simply crosstalk occurs when a photon or charge carrier from one pixel escapes and enters a neighbouring pixel where it triggers a second avalanche discharge. This effect is undesirable, but unfortunately is present in every SiPM device and scales with the reverse bias. An estimate of the crosstalk probability could be made from the ratio between the dark count rates at a 1.5 ph.e. threshold level and the dark rates at 0.5 ph.e. threshold level. Fig. 5.9 presents the obtained results. There is a good agreement with similar measurements performed by other groups [31].

5.3 SciFi Ribbon

A SciFi ribbon for the Mu3e experiment consists of 3 to 5 layers of scintillating fibres staggered as tightly as possible. The ribbons tested in this thesis were produced with a set of tools developed by the DPNC mechanical group (see Fig. 5.10). They include two teflon channels with a fixed 16.1 mm width and a u-type profile and one channel with 8.1 mm width, aluminium bars with teflon cover matching the profiles of the channels and assisting instruments like tweezers, scissors etc.

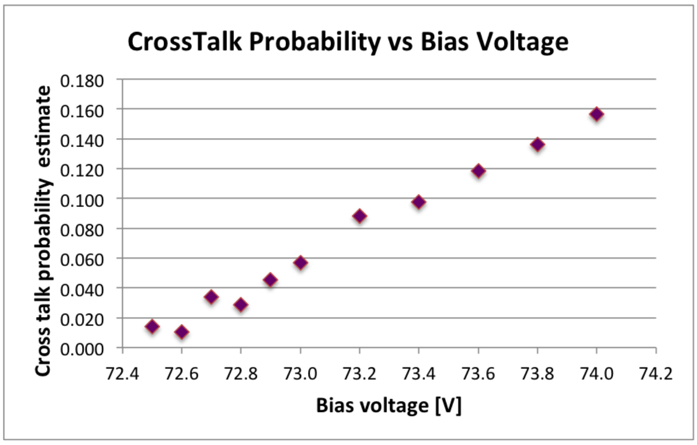

Figure 5.9: Cross-talk probability as a function of the applied bias voltage. The ratio of the dark counts rate at 1.5 ph.e. level to 0.5 ph.e. level was taken as an estimate for the probability.

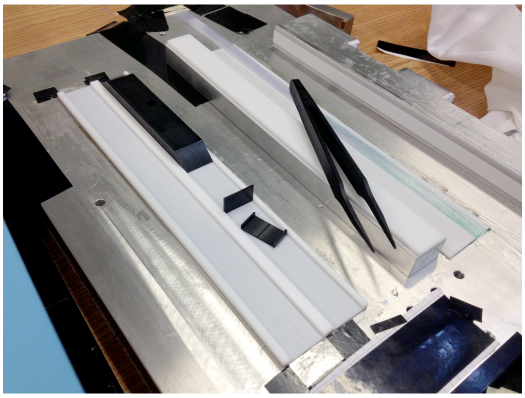

(a) Teflon channels on a flat surface and a bar matching their are used to align the fibres in a ribbon and reduce the unnecessary amount of glue

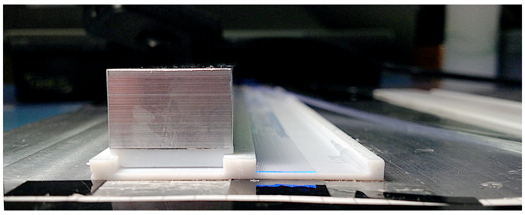

(b) Cross-sectional view of the teflon channels and the bar. The width of the channels is 16.1 mm

Figure 5.10: All the necessary tools used for the construction of a ribbon

Method to produce the ribbons

A rectangular channel made of teflon with dimensions 16.1mm×2mm×200mm constrains the first layer of 64 fibres. The channel is placed horizontally and the fibres are fixed at one of their ends. Afterwords, a thin layer of low viscosity glue and long curing time is spread over the fibres. A teflon bar brought on top of them and slid along their length removes the unnecessary amount of glue. The bar is with the same width and length as the channel profile - 16.1mm×200mm. As the fibres are plastic and only 250 μm in diameter they could easily cross each other. Both the glue and the bar assist in the proper alignment of the fibres: the bar allows an equal pressure to be applied on all fibres simultaneously, while the glue serves as "grease" and facilitates the correct placement of the individual fibres. It is verified by eye that there is no crossing and that no fibres were broken during the alignment process. If a fibre is not broken it is transparent, on points where the cladding is damaged spots of blue scintillating light are clearly visible. When the glue is completely dry a second layer consisting of 63 fibres is aligned above the first. The top fibres fall in the shallow gaps formed by the fibres form first layer. Additionally, when a fresh glue is applied over the second layer it reacts with the leftovers from the first layer, so by pressing a little harder the bar over the second layer the extra glue between the layers is pushed away. As a result, the thickness of the ribbon is reduced. The subsequent layers are added analogously. To keep the integrity of the ribbon after detaching it from the teflon bed, and to ease the polishing process, rectangular brackets hold the two ends. Photos of a ready ribbon with its cross-section are shown in Fig. 5.11.

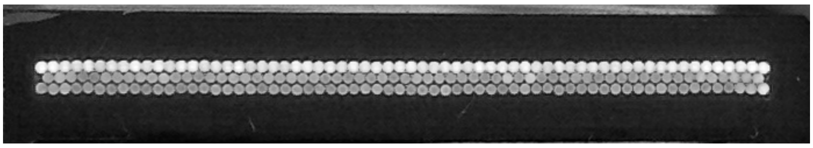

(a) Cross-sections of 16 mm wide ribbon with 64 fibres in the first layer

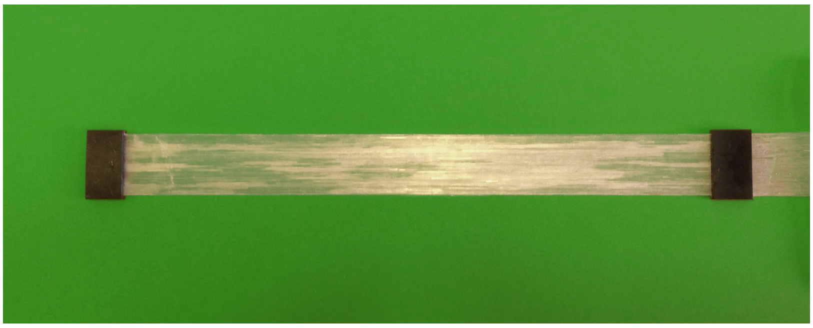

(b) Longitudinal view of a 16 mm ribbon

Figure 5.11: Photos of the first 16 mm wide ribbon. The uniform staggering of the fibres in clearly visible in the cross-section photo.

Several 8 mm wide ribbons were built during the initial tests of the aforementioned technique. Performance studies were carried out later with one of the first 8 mm ribbons. Two SiPM detectors were attached at both ends as shown in Fig. 5.12. After one of the detectors was glued, the alignment of the second was done with the help of a standard desk lamp illuminating the backside of the first detector.

Single fibre readout connector To prove the feasibility of a single fibre readout design, we attached a connector with holes of 300 μm in diameter and center to center

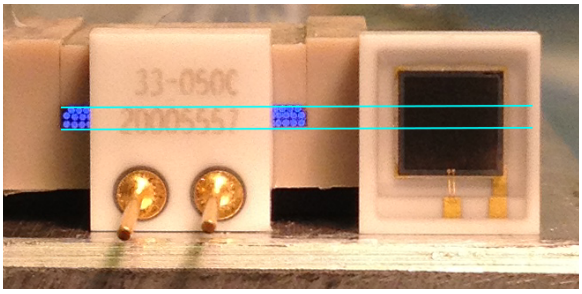

(a)

(b)

Figure 5.12: SiPM attached to a ribbon

distance of 500µm. Photos of a ribbon with the connector are presented in Fig. 5.13.

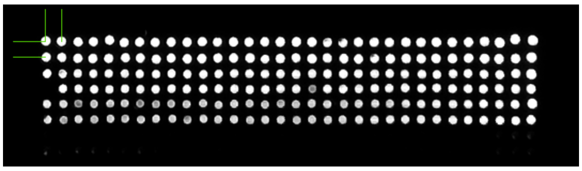

(a)

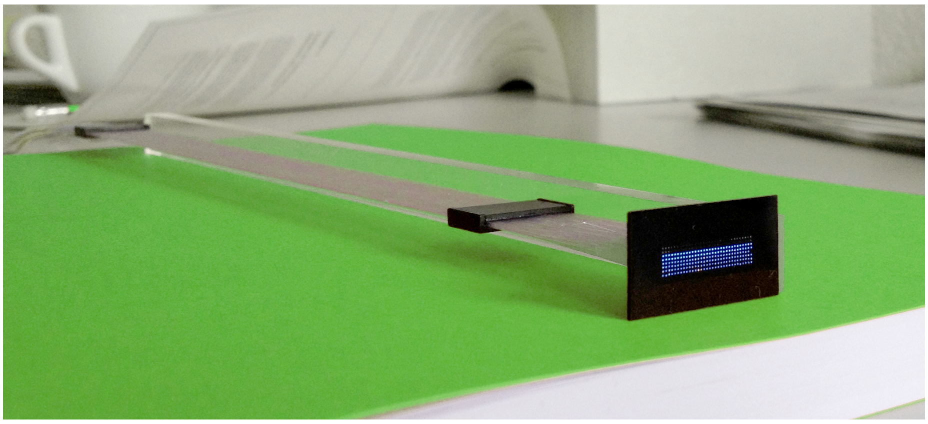

(b)

Figure 5.13: Photos of Sci-Fi ribbon with a connector considered for a single fibre readout

Chapter 6

Performance Results

First performance measurements and results are presented in the chapter. Characteristics of a three layer scintillating fibre ribbon readout by two 3×3 mm^2 SiPMs have been studied.

6.1 Experimental Setup

A collimated radioactive source ^{90}Sr provides electrons for the measurement performed in this work. The ^{90}Sr isotope is in equilibrium with its daughter product ^{90}Y, also a β^- emitter. Their electron spectrum is characterized by an end-point energy of 546 keV for ^{90}Sr and 2.28 MeV for ^{90}Y, sufficient to pass through the less than a millimetre thick ribbon. Electrons passing through the scintillating material deposit energy which is afterwards converted to light. Part of the photons propagate within the fibres until they reach the photon detectors placed at the ends. Two identical SiPMs, S10362-33-050C by Hamatsu, mounted on $DPNC286\_07A$ pre-amplifying boards collect the light from the fibres. The ribbon together with the pre-amplifiers and the source are placed inside a light isolated box. After amplification, the signals from the detectors are taken out trough connectors on the sides of the box and sent for processing to an acquisition system (see Fig. **??**). Each SiPM signal is split into two, one half enters an analogue to digital converter (ADC) and the other half goes through a discriminator to the stop of a time to digital converter (TDC). A scintillating bar placed underneath the ribbon serves as a trigger for the system. The bar is made of a plastic scintillator with dimensions 5mm×5mm×200mm and two SiPM sensors identical to the ones on the ribbon detect the light produced inside the bar. The bar and the ribbon cross each other at 90^o as shown in Fig. 6.2. The radioactive source is centred over the crossing point. When an electron passes through both the ribbon and the bar it triggers the system and a timing module generates a gate for the ADC and TDC. In the ADC module, the gate determines the period over which the incoming signal is integrated. The TDC module is operated in common start mode, so the gate signal initiates a start for counting the time until the arrival of a stop signal in each channel.

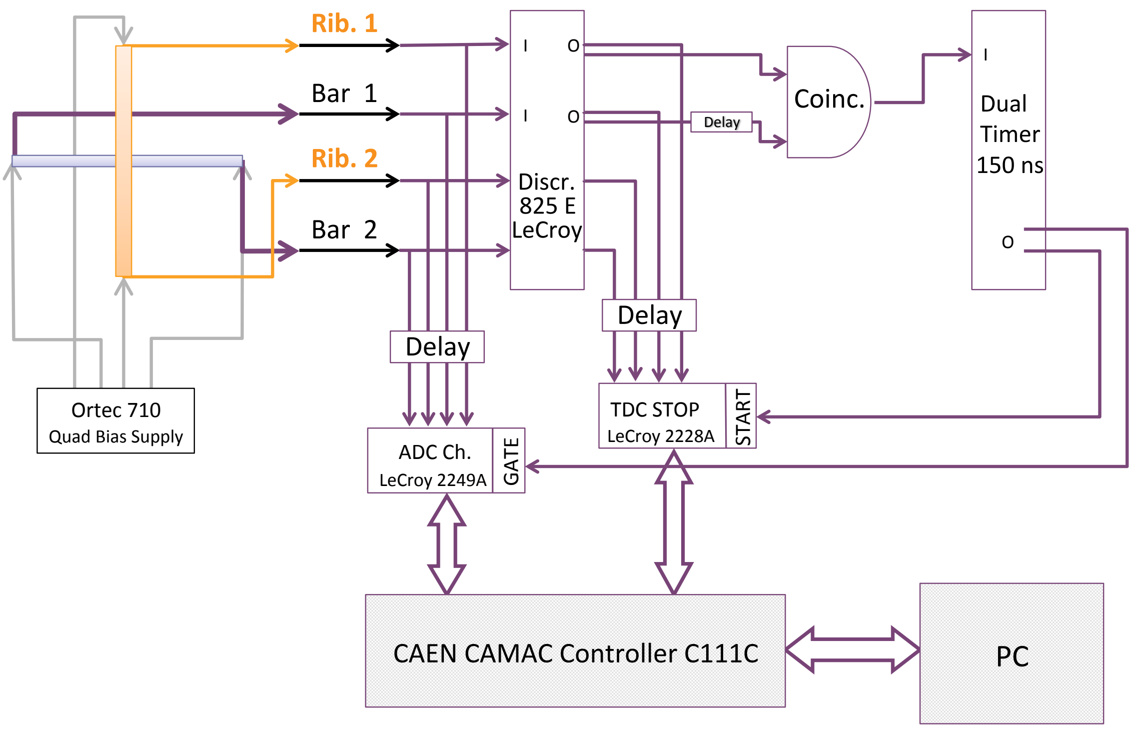

Figure 6.1: A schematic of the data acquisition system utilized for the measurements presented in this work

Trigger logic

The radioactive source is placed at distance of about 1 cm from the ribbon and is collimated through a 3 mm in diameter plastic collimator. The dispersion of the electrons at the ribbon level due to the finite size of the collimator is approximately 5 mm. If the electrons scattering off the edges of the collimator are taken into account, the particles going out of the source spread over even a larger region. To study the properties of the ribbon one needs to ensure that the photons detected by the detectors at the ends of the ribbon originate from the same interaction. One way

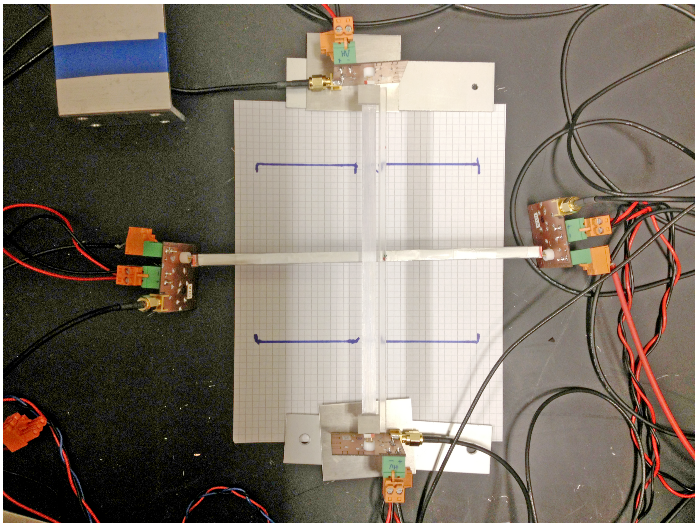

Figure 6.2: A thick scintillating bar placed beneath the ribbon serves as a trigger of the acquisition system

of implementing such trigger is by requiring a minimum number of photons to be detected simultaneously in the photon detectors at the two ends of the bar. Since the ribbon is 8 mm wide, if an electron reaches the bar underneath, it must have crossed the ribbon first. Unfortunately, the sensitive width of the ribbon is only 3 mm, so more than half of the particles that pass through the bar can not be detected by the SiPMs on the ribbon. Suppose, however, that there is, simultaneously, light at one end of the ribbon and at one of the bar's end, then one and the same particle passed through the sensitive part of both of them. Since, the output of the SiPM sensors is proportional to the number of detected photons, a discriminator could be used to select only events which have more than a fixed number of photons (e.g. 3) detected. If the amplitude of the analogue signal is high enough to pass the discriminator threshold, a negative NIM signal with a start determined by the start of the analogue signal is produced. Discriminator signals resulting from one end of the ribbon and the bar are sent to a coincidence module. This module generates an output if two input pulses overlap in time. The start of the coincidence signal is determined by the arrival of the latest pulse. In general, the two signals (one from the ribbon and the other from the bar) could arrive in the coincidence unit in an arbitrary order since all the cabling, and the SiPMs themselves, are identical. However, such freedom of the arrival time is undesirable when timing measurements are performed. By studying the signals on an oscilloscope, it was determined that the signal which initiates the trigger should be delayed by $\sim$10 ns, and the width of the signal arriving first should be extended to $\sim$30 ns. As a result, the signal from the bar i.e. the delayed signal is always second and the trigger start is determined by its arrival (see Fig. 6.3). The digitized timing value that a TDC module returns is equal to the difference between a start and an end time signals. In this case the start for all TDC channels is the start of the trigger and the stop in each channel is set by the delayed output of the discriminator channels. If the second signal is always the one from the bar, the TDC would return a single value for the time difference between the start and the stop in the corresponding channel in all the measurements. This difference is predetermined by the length of the cables used to transport the signals to the TDC. Indeed, in the time histogram of the channel that triggers the system we observe a sharp peak with a single channel width.

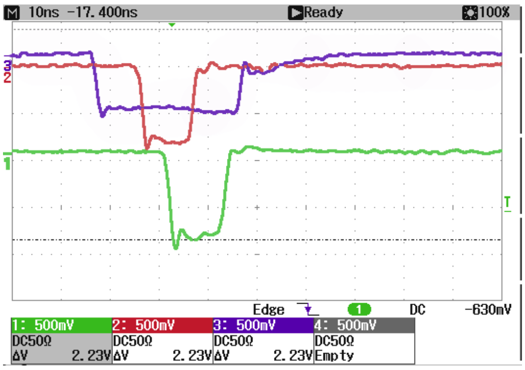

Figure 6.3: Coincidence logic used for triggering on the arrival of signals from one end of the ribbon and one end of the bar. The red signal is the one from the bar with added delay such that it always arrives after the signal from of the ribbon (purple). The green signal is the output of the coincidence unit

6.2 ADC Spectra

In the following section characteristics of a general ADC spectrum from the ribbon are discussed. An efficiency study based on the longitudinal position of where the electrons interact with the fibre is also presented.

6.2.1 Characteristics of a SiPM Spectrum

Fig. 6.4 is an example of an ADC spectrum obtained from one of the SiPM detectors attached to the ribbon. It was produced with reverse bias on the SiPMs set to the operational values provided by the manufacturer (72.7 V for all the sensors used in this work). The trigger logic discussed prior in the text was implemented during the measurements. The spectrum is from the detector whose signal was not involved in the triggering. As evident from the measurements with an oscilloscope, the spectrum has a discreet structure where each peak represents the number of photons detected. The peak on the very left end of the spectrum (coloured in red) is the so called SiPM pedestal. It arises from the thermal motion of the electrons in silicon and is present even if no light is incident on the device. The second peak corresponds to a photon being detected in one pixel, the third peak - to photons starting avalanches in two pixels, and so on. There is no information on which pixel has fired as all of them are connected to the same output, however the equidistant and narrow peaks in the ADC spectrum indicate that all pixels respond in a similar manner to the incident photons. Each peak has approximately Gaussian shape, so the centroid, i.e. their amplitude [1], could be determined by fitting. Their spacing is constant and depends linearly on the ADC channels (see Fig. 6.5). Sometimes an electron from the avalanche in one pixel escapes and triggers a Geiger discharge in a neighbouring pixel. When the electrons from the first pixel reach the collecting electrodes the voltage over the device starts decreasing due the quenching resistor. As a consequence, the discharge in the secondary pixel results in a fewer number of electrons arriving at the collecting electrodes, and thus produces a signal with smaller than a single pixel amplitude. The net effect is a plateau under the separate peaks in the ADC spectrum. Additional smearing of the peaks occurs with increasing the number of fired pixels since each peak is a sum of the signals from several pixels. An approximate expression for the width of the n^{th} peak is given by $\sigma_n = \sqrt{n\sigma^2 + \sigma^2_{pedestal}}$ [32], where σ is the spread of the signals produced by different pixels and $\sigma_{pedestal}$ is the width of the pedestal peak. For a large n, the peaks overlap and the spectrum loses its "discreet" structure. The effect is present in the spectrum in Fig. 6.7 taken with one of the SiPM detectors coupled to the scintillating bar. The number of photons produced in the bar is much larger than those in the thin fibres, and thus the number of fired pixels at the detector is much larger. The use or a radioactive source like the ^{90}Sr allows electrons with very low energy to stop in the bar and generate only a few photons which explains the peaked shape at the beginning of the spectrum. If the electrons passing the bar were minimum ionizing particles (MIP) the shape of the spectrum would follow a Landau distribution. However, the wide energy range of the source electrons and the large thickness of the bar result in a non-Landau shaped spectrum. The bias applied to the SiPMs on the bar is the same as that of the SiPMs on the ribbon and the

[1] The digitized values that the current ADC module returns are proportional to the integral over time of an incoming analogue signal, which is in turn proportional to the amplitude of the signal.

the spectrum is produced with the same ADC module. The reason that the peaks in this spectrum appear closer to each other is because the signal from the detector was attenuated by 6dB prior to entering the digitizing module.

In Fig. 6.6 the red ADC spectrum is from a SiPM detector that triggers the system. The grey coloured histogram is added for completeness and represent the full spectrum of the same detector when the trigger is initiated by the opposite SiPM attached to the ribbon.

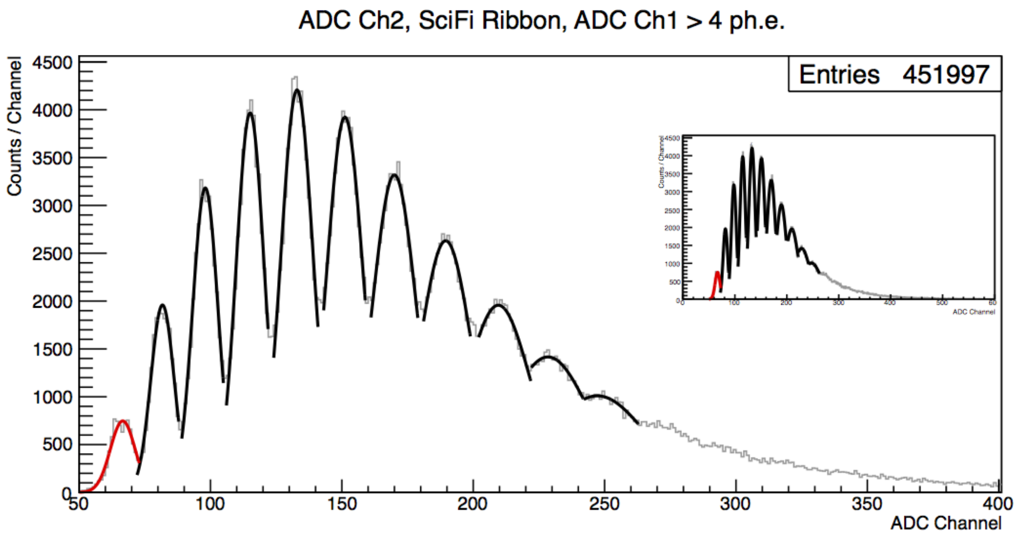

Figure 6.4: An ADC spectrum from one of the SiPM detectors attached to the ribbon. The signal is from the detector that does not participate in the trigger logic. The red coloured peak is the pedestal of the SiPM device and the first peak to the right of the pedestal is the one corresponding firing of one pixel

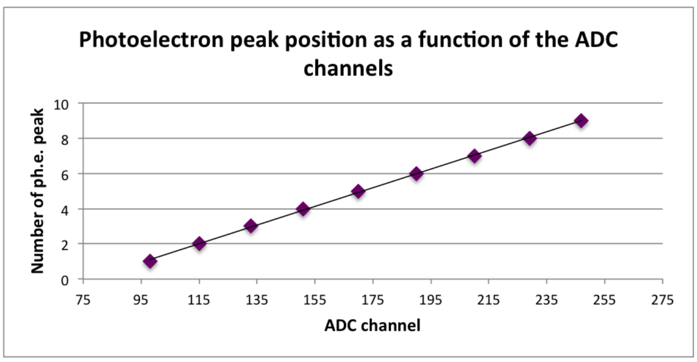

Figure 6.5: The photoelctron peaks in the ADC spectrum of a SiPM are equidistant, so they are linear with the ADC channels

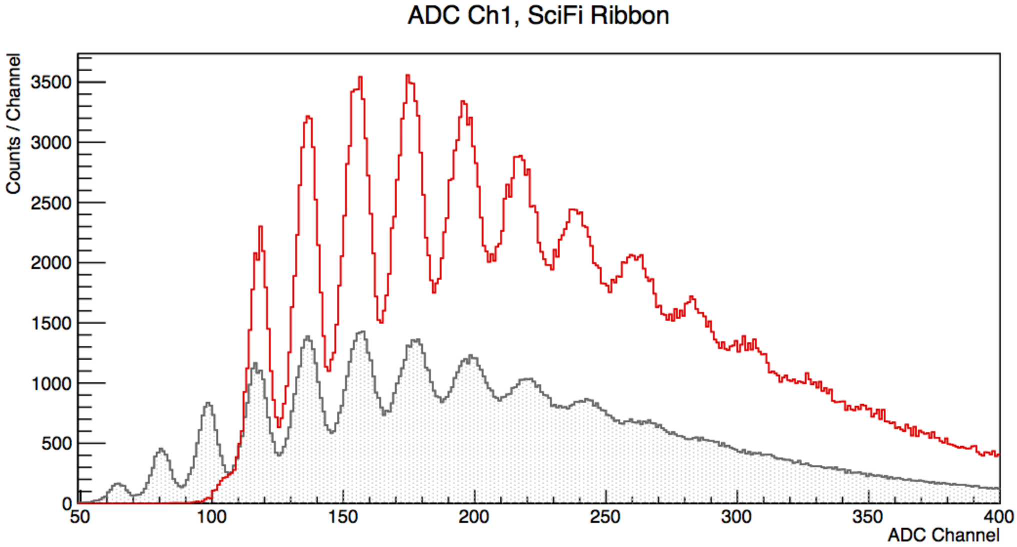

Figure 6.6: An ADC spectrum of a SiPM detector when used (red) or not (grey) in the trigger. The signal from the detector passes a discriminator threshold in order to generate a trigger so the lowest amplitudes are absent from the data

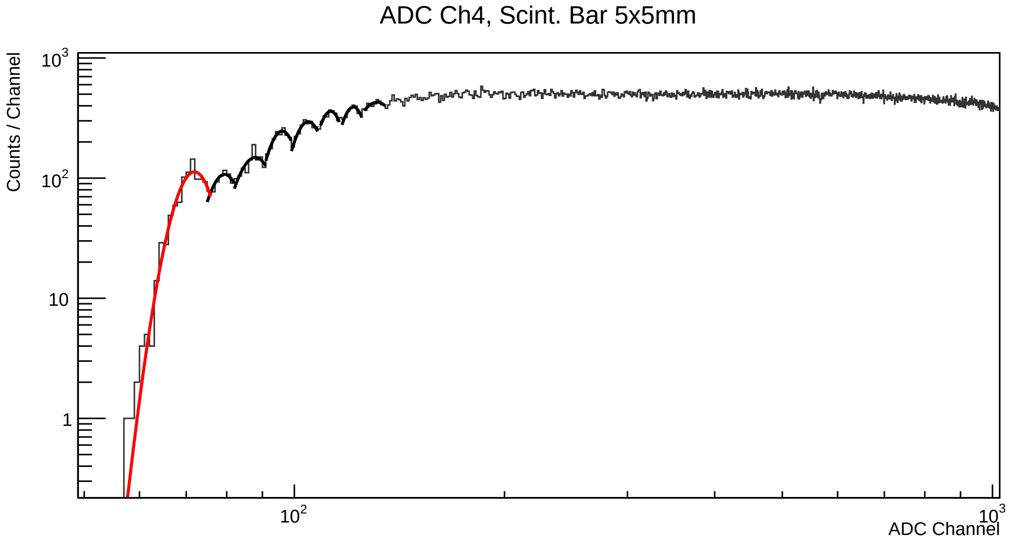

Figure 6.7: ADC spectrum gathered with one of the SiPMs glued to the scintillating bar. The number of photons in the bar is very high compared to that of the ribbon so the "discreet" structure of the spectrum smears after the low ADC channels

6.2.2 Efficiency of the Ribbon-SiPM System

The studies presented hereafter are the first steps towards determining the efficiency of the time-of-flight fibre module. The relations between the number of photons detected at each end of the ribbon are investigated.

Photons produced as a result of an electron passing through a fibre are emitted isotropically around the interaction point. As a consequence, approximately the same number of photons confined in the fibre propagate in the two opposite directions. The simulation studies discussed earlier point that once captured the light propagates predominantly in the cladding. The fibres are much shorter than the attenuation length of the material they are made of, so we expect the same amount of light to reach both ends. If n photons are detected on one side the probability of having at least one or two photons detected on the other side is a measure of the efficiency of the ribbon-SiPMs system.

Fig. 6.8 shows how the ADC spectrum of one of the detectors changes with the number of photons registered in the opposite detector. The maximum of the spectrum shifts to the right when more photons are detected at the other end of the ribbon . The overall shape, however, remains unchanged since the process of detecting photons incident on a SiPM device is of Poissonian nature.

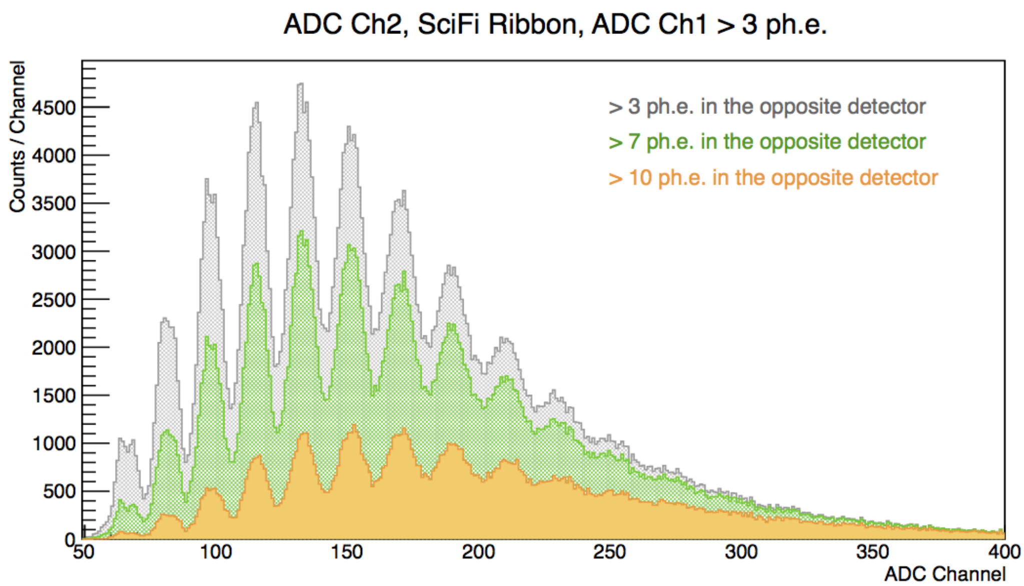

Figure 6.8: The maximum of the ADC spectrum from one of the ribbon detectors shifts to the right with the increasing number of photons detected in the opposite SiPM.

The inefficiency of the system is determined by the number of events that fall in the pedestal peak of the ADC spectrum. To study the efficiency of one of the SiPM detectors over a varying number of photoelectrons generated in an opposite SiPM sensor we applied the cuts marked with red lines in Fig. 6.9. Furthermore, the source was moved to three different positions in order to test the effects when the interaction

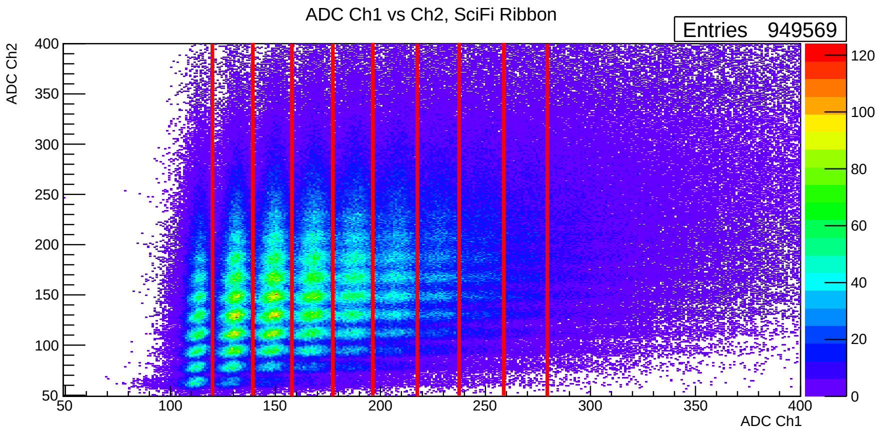

Figure 6.9: Relation between the ADC spectra of the two SiPM detectors at the ends of the ribbon. The probability of having more photons detected in one of the detectors increases when there is more light incident on the other. The red lines indicate the cuts applied on one of the detectors to study the performance of the other. The peaks of the spectrum correspond to a fixed number of firing SiPM pixels.

point is near the triggering detector, far from it or in the middle between the two ends of the ribbon. The results are summarized in Fig. 6.10.

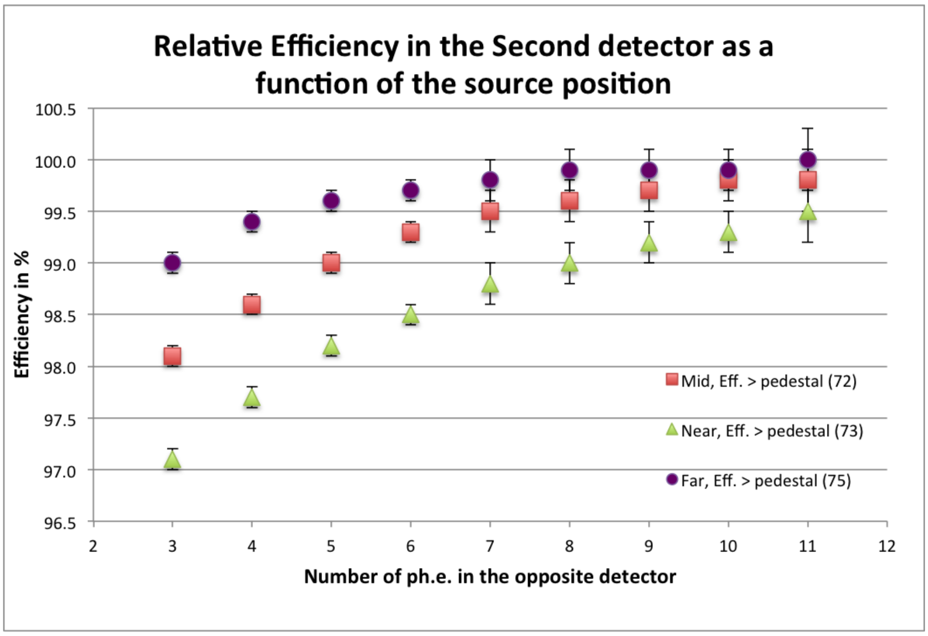

Figure 6.10: Relative efficiency of the ribbon provided a given number of photons is detected at one of the ends. The efficiency is defined as the number of events in the pedestal divided by the total number of events satisfying the conditions. The more light incident on one of the detector the better the probability of having pixels firing in the other detector is.

When the number of detected photons increases on one side, the probability of having no signal on the other side decreases, thus the efficiency of the system improves. The best results are achieved when the electrons interact with the ribbon far from the triggering side. Combined with the fact that the inefficiency of the second detector is greatest when the point of interaction is far from it, these results indicate that there are different amounts of light travelling in both directions of the fibre is not exact. It might be explained by the refraction index of the glue, which is higher than that of the outer layer of the cladding. As a result some photons could escape the ribbon. To test the validity of such an argument, though, alternative types of adhesives should be tested and probably even the use of reflective paint. One should keep in mind that any unnecessary layer of material is an obstacle for the tracking module, so paint and high viscosity adhesives must be avoided whenever possible.

6.3 Time Measurements

TDC Calibration The TDC module was calibrated using a pulse generator. A signal from the generator enters a logic Fan-In/Fan-Out module which duplicates its input to three output channels. One of them goes to a gate generator and serves as a start for the TDC module and the other two are delayed with a known difference between them and enter as stop signals in two channels of the TDC. The module is linear with the time difference between the start and the stop signals as well as with the time difference between two channels as shown in Fig. 6.11. By linear fitting it is found that one TDC channel corresponds to ~ 45 ps.

TDC output with SiPM signals The time-to-digital converter model LeCroy 2228a has 8 channels and for each of them returns a single value t_i proportional to the time difference between a start and a stop signal. For input were used NIM signals generated by a leading edge compensated discriminator LeCroy 825E. The discriminator, on the other hand, processes the analogue SiPMs pulses. It uses two threshold levels - one is the so called timing threshold which is usually set just above the noise level and the other is the amplitude threshold which determines the minimum amplitude required to pass the discriminator. The jitter of the time signal is determined by the difference in the slopes of the signals just above the noise level. One additional parameter - delay time - takes into account the rise time of the signals.

For the present measurements one signal was used as a common start for all channels. It was produced with a timing module as result of the trigger conditions.

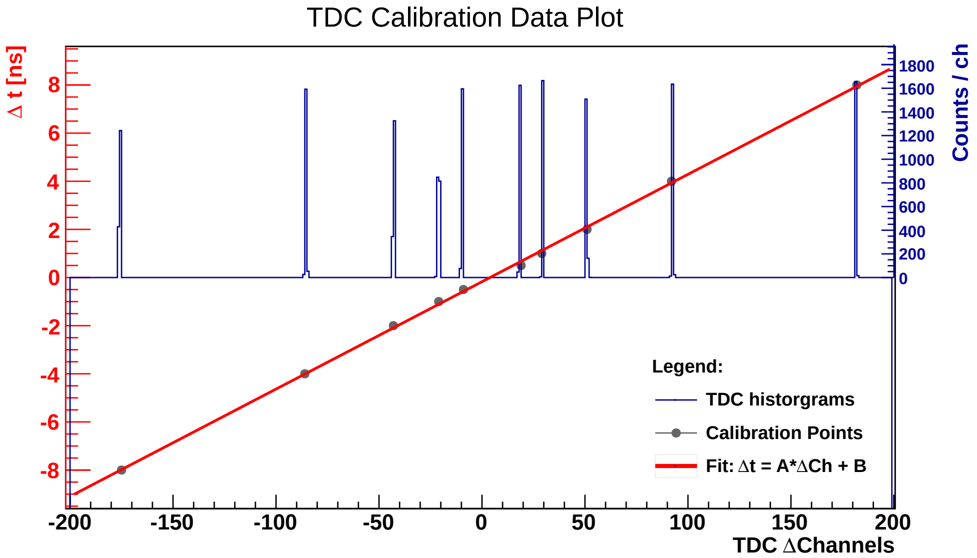

Figure 6.11: Results from the TDC calibration. The blue histogram is data collected with the module. The single channel structure indicates that the module operates properly. Its resolution per channel is measured to be ~ 45 ps

The output of a single channel is then simply $t_i = T_i - T_0$, where T_0 is the arrival time of the start signal and T_i - the arrival of the stop signal. Let T_1 be the arrival time of one of the SiPMs signal and T_2 - the arrival time of the other SiPM. The time difference between the two outputs of the TDC is independent of T_0:

$$\Delta t = t_1 - t_2 = T_1 - T_0 - T_2 + T_0 = T_1 - T_2$$

Additionally, the individual signals from the two SiPM detectors are independent and both follow a normal distribution. Hence, their difference is also a Gaussian distributed variable. The term time resolution in this work refers to the standard deviation σ of a Gaussian variable. For the above expression the standard deviation of the variable Δt is equal to $\sigma_{\Delta t} = \sqrt{\sigma_1^2 + \sigma_2^2}$, where σ_1 and σ_2 are the intrinsic resolutions of the two SiPM detectors. The time difference resolution $\sigma_{\Delta t}$ is derived from the data and it can be used to estimate the intrinsic detector resolution.

Since the two detectors are identical, it is natural to assume that their intrinsic time resolutions are equal. For simplicity we denote $\sigma_1 = \sigma_2 = \sigma$ and express the time resolution σ in terms of the time difference resolution:

$$\sigma_{\Delta t} = \sqrt{\sigma_1^2 + \sigma_2^2} = \sqrt{2\sigma^2} \quad \Rightarrow \quad \sigma = \frac{\sigma_{\Delta t}}{\sqrt{2}}$$

In the Mu3e experiment the times from the two ends of a single ribbon will be averaged to give the moment at which an electron passed through the fibres, thus the resolution of one ribbon becomes:

$$\sigma_{MT} = \sqrt{\frac{\sigma^2}{2}} = \frac{\sigma_{\Delta t}}{2}$$

A study of the time resolution as a function of the detected photons in the two SiPMs was made. Cuts were applied in the analysis software after collecting the data. The cut conditions require at least n photons to be detected simultaneously at both ends of the ribbon. Fig. 6.12 presents several time difference histograms obtained for different number of photons registered in the detectors. The most forward histogram (in orange) corresponds to the highest minimum number of photons observed in a detector. It was required the more than 11 ph.e. triggered a discharge in each of the SiPMs.

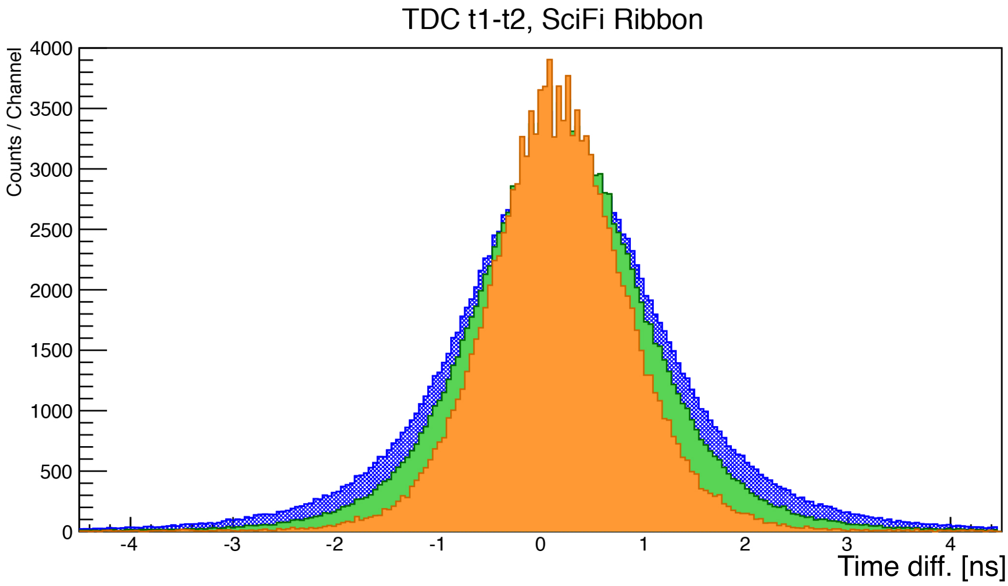

Figure 6.12: Time difference between the two SiPM detectors on the ribbon. The histograms are scaled to match the amplitudes. The blue one is obtained with conditions of having at least 3 ph.e. detected at both ends, the green - at least 7 ph.e., and orange one - at least 11 ph.e

To extract the resolution, the time difference spectra were fitted with Gaussian functions. Histograms with the fits and their components are plotted in Fig. 6.13. The sum of the blue and red curves leads to a fit that best describes the data, with the narrow (red) Gaussian representing the time difference of the two signals.

For the three different positions of the source time histograms with cuts ranging from 4 to at least 11 photons were constructed and fitted with Gaussian functions.

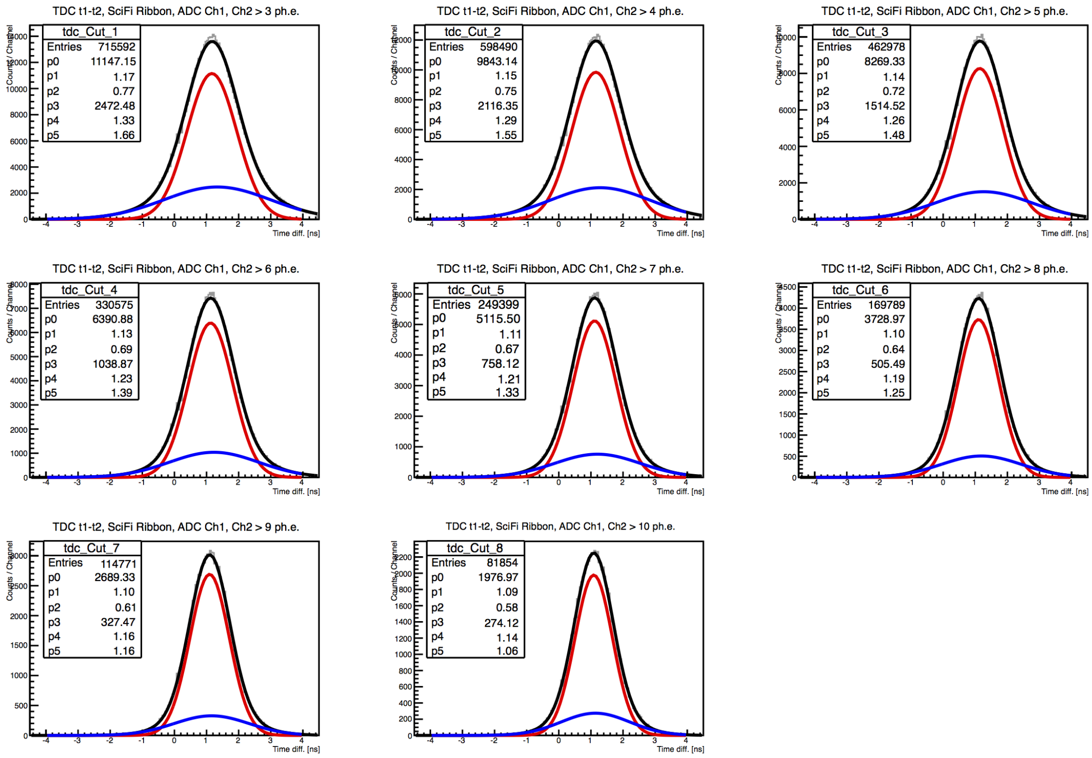

Figure 6.13: Time difference between the two SiPM detectors on the ribbon for different number of photons detected simultaneously in both SiPM sensors. The width of the histograms narrows down when more photons produced photoelectrons in the SiPM sensors. The resolution $\sigma_{\Delta t}$ is equal to the width of the narrow (red) curves.

Fig. 6.14 reports on the results from the fits. The time resolution improves when there is more light incident on the SiPM detectors. The data shows that for ten photons the resolution of the ribbon is $\sigma_{MT} = \frac{\sigma_{\Delta t}}{2} \approx 300$ ps which is better than the required resolution of 500 ps for the Mu3e fibre hodoscope. The graph in Fig.6.15 shows the fraction of events for which the time resolution is around 300 ps is less than 20%.

To test the performance of the ribbons when operated at high rates, additional studies with beam particles should be conducted.

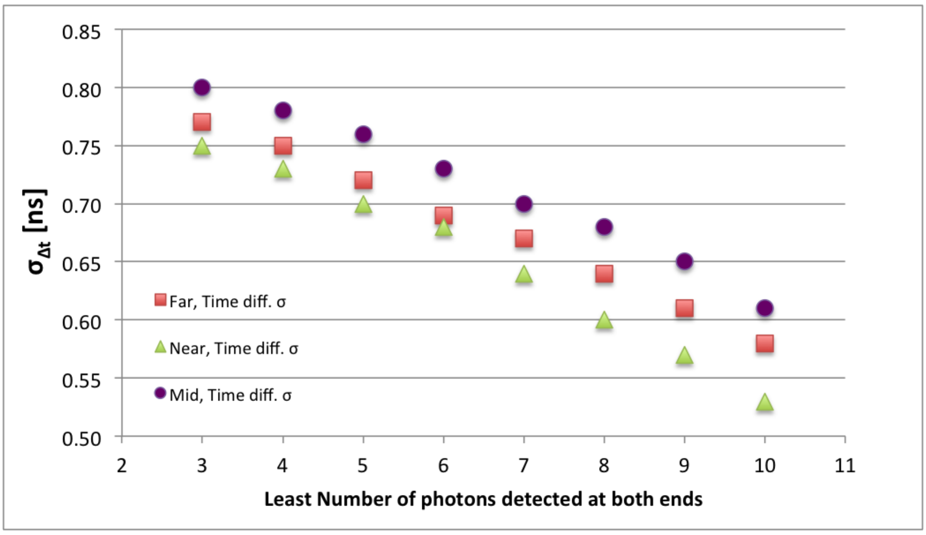

Figure 6.14: Resolution of the time difference between the two detectors at the ends of the ribbon. The behaviour of the points proves that the time resolution improves with the number of photons detected.

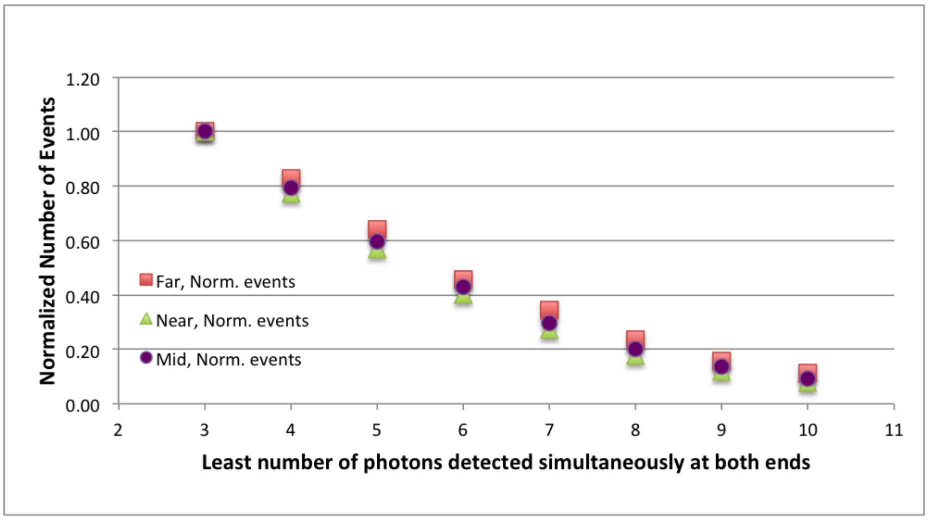

Figure 6.15: Number of events for which there was at least n photons detected simultaneously at both ends of the ribbon. The events are normalized to the number of events where at least three photons were detected at both sides.

Chapter 7

Summary

With a sensitivity of 10^{-16}, the Mu3e experiment will search for the lepton flavour violating decay $\mu^+ \to e^+e^-e^+$. The most recent experimental results exclude this process with BR($\mu^+ \to e^+e^-e^+$)<1×10^{-12} at 90% C.L. [2]. Multiple theories beyond the Standard Model, however, predict its existence with branching ratio just below the experimentally determined limit. A precision study like the proposed Mu3e experiment opens possibilities to test these theories and look for new physics at mass scales in the range of PeV, far beyond the reach of any direct measurement available today.

An important factor in reaching the projected sensitivity is the ability of the experiment to isolate true events from accidental and irreducible background sources.This is only accessible by a detector with excellent momentum and time resolutions. A spectrometer placed inside a magnetic field is proposed for this purpose. It consists of a silicon tracker based on HV-MAPS pixel sensors and a time of flight detector built from scintillating fibres and SiPM detectors. The geometrical configuration is optimized for measuring electrons with momentum ranging from several MeV up to half the muon mass i.e. 53 MeV. Within this energy range the momentum resolution of the tracker is mainly deteriorated by multiple scattering of the electrons in the detector modules. To minimize these effects the material budget is kept as low as possible. Unfortunately, the reduced material worsens the time resolution of the scintillating fibre hodoscope.

The performance of ribbons made of three layers staggered plastic scintillating fibres with ⌀250 μm was studied. The ribbons were built and their efficiency was analysed in the scope of this thesis. Initial tests with radioactive source ^{90}Sr indicate that a system readout by two $3{\times}3$ mm^2 SiPMs attached to the ends of one ribbon could provide time information with resolution of 500 ps when as little as three photons are detected at both sides. When the number of detected photons at both ends is increases up ten, the time resolution improves to 300 ps. Such events, however, amount to less than 20% of all detected particles. It was also found that when a photon is detected in one of the SiPMs the probability of seeing a signal in the opposite photon detector is more than 90%. These results are compatible with the Mu3e requirements, however, further studies in conditions with higher particle rates and with better acquisition system should be conducted.

List of Figures

Bibliography

[1] Research proposal for an experiment to search for the decay $\mu \rightarrow eee$, Dec 2012.

[2] U. Bellgardt et al. Search for the Decay $\mu^+ \rightarrow e^+e^+e^-$. *Nucl.Phys.*, B299:1, 1988.

[3] CERN. New results indicate that new particle is a higgs boson. http://home.web.cern.ch/about/updates/2013/03/new-results-indicate-new-particle-higgs-boson.

[4] http://en.wikipedia.org/wiki/file:standard_model_of_elementary_particles.svg, February 2013.

[5] F. Halzen and A. D. Martin. *Quarks and Leptons: An Introductory Course in Modern Particle Physics.* John Wiley & Sons, 1984.

[6] J.C. Street and E.C. Stevenson. New evidence for the existence of a particle of mass intermediate between the proton and electron. *Phys. Rev.*, 52:1003–1004, 1937.

[7] K. Nakamura et al. Review of particle physics. *J. Phys.*, G37:075021, 2010.

[8] Y. Fukuda et al. Evidence for oscillation of atmospheric neutrinos. *Phys. Rev. Lett.*, 81:1562–1567, 1998.

[9] K. Abe et al. The T2K Experiment. *Nucl.Instrum.Meth.*, A659:106–135, 2011.

[10] Q. R. Ahmad et al. Measurement of the charged current interactions produced by b-8 solar neutrinos at the sudbury neutrino observatory. *Phys. Rev. Lett.*, 87:071301, 2001.

[11] F.P. An et al. Observation of electron-antineutrino disappearance at Daya Bay. *Phys.Rev.Lett.*, 108:171803, 2012.

[12] Y. Kuno and Y. Okada. Muon decay and physics beyond the standard model. *Rev. Mod. Phys.*, 73:151–202, 2001.

[13] J. Adam et al. MEG Collaboration. New constraint on the existence of the $\mu^+ \to e^+\gamma$ decay. *arXiv:1303.0754 [hep-ex], Online eddition*, 2013.

[14] W. Bertl et al. A search for $\mu - e$ conversion in muonic gold. *Eur. Phys. J.*, C47:337–346, 2006.

[15] R. Tschirhart. The Mu2e experiment at Fermilab. *Nucl.Phys.Proc.Suppl.*, 210-211:245–248, 2011.

[16] Y.G. Cui et al. Conceptual design report for experimental search for lepton flavor violating mu- - e- conversion at sensitivity of 10^{-16} with a slow-extracted bunched proton beam (COMET). 2009.

[17] A. Kurup. The COherent Muon to Electron Transition (COMET) experiment. *Nucl.Phys.Proc.Suppl.*, 218:38–43, 2011.

[18] Y. Kuno. Lepton flavor violation: Muon to electron conversion, COMET and PRISM/PRIME at J-PARC. *PoS*, NUFACT08:111, 2008.

[19] J. Pasternak, L. Jenner, Y. Uchida, R. Barlow, K. Hock, et al. Accelerator and Particle Physics Research for the Next Generation Muon to Electron Conversion Experiment - the PRISM Task Force. WEPE056, 2010.

[20] Y. Amhis et al. Averages of b-hadron, c-hadron, and tau-lepton properties as of early 2012. 2012.

[21] William R. Leo. *Techniques for Nuclear and Particle Physics Experiments.* Springer, 1994.

[22] I. Peric. A novel monolithic pixelated particle detector implemented in high-voltage CMOS technology. *Nucl.Instrum.Meth.*, A582:876–885, 2007.

[23] Mu3e Collaboration. Mu3e wiki. http://www.physi.uni-heidelberg.de/Forschung/he/mu3e/wiki/index.php.

[24] Hamamatsu Photonics. Catalog of mppc devices. http://www.hamamatsu.com/us/en/product/category/3100/4004/index.html.

[25] R. Greim et al. A high-resolution scintillating fiber tracker with sipm array readout for cosmic-ray research. Talk at RWTH Aachen University, 2009.

[26] S. Ritt, R. Dinapoli, and U. Hartmann. Application of the DRS chip for fast waveform digitizing. *Nucl.Instrum.Meth.*, A623:486, 2010.

[27] G. F. Knoll. *Radiation Detection and Measurement.* John Wiley & Sons, 2000.

[28] Kuraray. Plastic scintillating fibres. http://kuraraypsf.jp/psf/sf.html.

[29] B. Dolgoshein et al. Status report on silicon photomultiplier development and its applications. *Nucl. Instr. and Meth. A*, 563:368–376, 2006.

[30] S. Uozumi. Development and study of the multi pixel photon counter. Talk at Vienna Conference on Instrumentation, 2007.

[31] B. Beischer et al. The development of a high-resolution scintillating fiber tracker with silicon photomultiplier readout. *Nucl.Instrum.Meth.*, A628:403–406, 2011.

[32] V. Balagura et al. Study of scintillator strip with wavelength shifting fiber and silicon photomultiplier. *Nucl. Instr. and Meth. A*, 564:590–596, 2006.

Acknowledgements

First of all, I would like to express my gratitude to Dr. Alessandro Bravar for giving me the opportunity to work on the Mu3e project and guiding me through the time spent at the University of Geneva.

I am also thankful to Yannick Favre for developing the electronic boards used for the SiPM readout and to the mechanical engineers at DPNC for assisting me in building the ribbons.

I appreciate the discussions with Yordan Karadzhov on the timing measurements and with Roman Gredig on the simulations of the experiment, and specifically on the timing hodoscope.

Furthermore, I am thankful to Prof. Divic Rapin for agreeing to be my second examiner.

I would like to thank all my friends and my family for their support. In particular, I thank Diana and Valentin for making my studies at the University of Geneva possible.

Finally, I thank Konstantin for believing in me and my work and encouraging me to follow my dreams.